Beam-inside-beam contact: Mechanical simulations of slender medical instruments inside the human body

Marco Magliulo[a], Jakub Lengiewicz[a,b], Andreas Zilian[a], Lars A.A. Beex[a,*]

[a] *Institute of Computational Engineering, Faculty of Science, Technology and Communication, University of Luxembourg, Maison du Nombre, 6, Avenue de la Fonte, 4364 Esch-sur-Alzette, Luxembourg*
[b] *Institute of Fundamental Technological Research of the Polish Academy of Sciences (IPPT PAN), ul. Pawinskiego 5B, 02-106 Warsaw, Poland*

Abstract

Background and Objective. This contribution presents a rapid computational framework to mechanically simulate the insertion of a slender medical instrument in a tubular structure such as an artery, the cochlea or another slender instrument.

Methods. Beams are employed to rapidly simulate the mechanical behaviour of the medical instrument and the tubular structure. However, the framework's novelty is its capability to handle the mechanical contact between an inner beam (representing the medical instrument) embedded in a hollow outer beam (representing the tubular structure). This "beam-inside-beam" contact framework, which forces two beams to remain embedded, is the first of its kind since existing contact frameworks for beams are "beam-to-beam" approaches, *i.e.* they repel beams from each other. Furthermore, we propose contact kinematics such that not only instruments and tubes with circular cross-sections can be considered, but also those with elliptical cross-sections. This provides flexibility for the optimization of patient-specific instruments.

Results. The results demonstrate that the framework's robustness is substantial, because only a few increments per simulation and a few iterations per increment are required, even though large deformations, large rotations and large curvature changes of both the instrument and tubular structure occur. The stability of the framework remains high even if the modulus of the inner tube is thousand times larger than that of the outer tube. A mesh convergence study furthermore exposes that a relatively small number of elements are required to accurately approach the reference solution.

Conclusions. The framework's high simulation speed originates from the exploitation of the rigidity of the beams' cross-sections to quantify the exclusion between the inner and the hollow outer beam. This rigidity limits the accuracy of the framework at the same time, but this is unavoidable since simulation accuracy and simulation speed are two competing interests. Hence, the framework is particularly attractive if simulation speed is preferred over accuracy.

*corresponding author: L.A.A. Beex, Lars.Beex@uni.lu

Keywords: surgical simulation, contact mechanics, beam-inside-beam, artery, cochlea.

1. Introduction

Mechanical simulations of surgical interventions can be used to train surgeons, reveal patient-specific complications that may occur during surgery and plan interventions patient-specifically. In the future, mechanical simulations of surgical interventions may even be used to optimize medical instruments for each patient (*e.g.* shape and stiffness) and be exploited to autonomously perform interventions.

Numerous frameworks to numerically simulate surgical interventions can be found in the literature. For instance, one set of frameworks simulates cutting through soft tissues in real-time [4–6, 34, 42] to provide haptic feedback to the trainee performing the "intervention". Another set of approaches aims to simulate the insertion of needles [2, 3, 8, 10, 36]. These frameworks may also be used to provide haptic feedback and/or to help to accurately steer the needle to the target of interest during surgery.

However, the framework presented in this contribution focuses on mechanical simulations that involve the insertion (or removal) of a slender medical instrument inside a tubular structure such as an artery, the cochlea or another slender instrument such as a catheter. In other words, our simulations do not involve the damaging of tissues due to cutting or needle insertion. The aim of this contribution is not to target one type of intervention in particular, but to present the first mechanically consistent formulation that can handle contact between one slender deformable body inside another slender deformable body, if both bodies are represented by beams.

Thus, the proposed framework is similar to the frameworks presented in [1, 9, 15, 27, 39] in which the insertion of guide-wires and catheters in arteries and the insertion of slender implants in the human cochlea are simulated. The difference between the proposed framework and the frameworks of [1, 9, 15, 27, 39] is that our framework represents both the slender medical instrument and the tubular structure as beams, whereas the frameworks of [1, 9, 15, 27, 39] only represent the slender medical instrument with beams whilst conventional 3D finite elements are used to represent the tubular structure.

A wide variety of schemes to handle contact between beams can be distinguished in the literature. All existing "beam-to-beam" contact frameworks are formulated to repel penetrating beams. Several of these beam-to-beam contact frameworks are only applicable if the beams' cross-sections are circular, shear deformations are ignored and the contact area remains small, since unilateral contact conditions are enforced at the closest pair of centroid points [33, 41, 43]. Thus, if two beams collide, a contact force is applied at the closest pair of centroid points to repel the two beams. If the beams' cross-sections are elliptical, the consideration of the centroid-lines alone is insufficient to determine the contact locations. Instead, contact forces must be applied at the closest pair of surface points where the tangent planes of the contacting surfaces are parallel. This was demonstrated by Gay Neto et al. [12, 13] for frictionless and frictional cases, respectively.

Furthermore, in case of non-localized contact (e.g. for parallel beams in contact), the assumption of point-wise contact does not hold. Meier et al. [30] have therefore proposed a contact framework to handle non-localized beam-to-beam contact, but the cross-sectional shape is restricted to (rigidly) circular and shear deformation is not accounted for. These

restrictions enable quantifying the penetration solely using the centroid-lines of the beams, which yields rapid simulations.

Magliulo et al. [28, 29] presented other master-slave frameworks for beam-to-beam contact applicable to both shear-deformable and shear-undeformable beams, with both circular as well as elliptical cross-sections. Both schemes consider the beam's surfaces explicitly, which has resulted in wider applicability than the scheme of Meier et al. [30], albeit at the expense of the simulation speed. A two-half pass algorithm was furthermore formulated in [29] to remove the bias of master-slave approaches for beam-to-beam contact, but with limited benefits for the results.

The beam conglomerates of interest to this contribution differ from the aforementioned works [28, 29], since the focus is on "beam-inside-beam" contact instead of "beam-to-beam" contact. In other words, the beams must remain embedded for the beam conglomerates of interest in our contribution, whereas existing beam-to-beam contact frameworks repel penetrating beams. The measure of penetration in our beam-inside-beam framework, on the other hand, shows similarities with the measure of penetration for the "beam-to-beam" contact framework of [28]. Penetration is measured between sections distributed along the inner beam and the interior surface of the outer beam. In case of contact, unilateral constraints are regularized with the penalty method, which brings compliance to the otherwise rigid cross-sections.

The outline of the remainder of this contribution is as follows. In Section 2, the contact framework is presented in the space-continuous setting along with the associated contact virtual work. Also in this section, spatial discretization applied to the finite element method is discussed. Contact kinematics and the contact virtual work are subsequently discretized. Implementation details are also included. The numerical examples of Section 3 indicate the promising capabilities of the contact framework. Section 4 discusses possible extensions and concludes this contribution.

2. Methods

2.1. Space-continuous contact formulation

The contact kinematics employed in this contribution are presented in this section [12, 13, 28, 29]. First, the beam's surface parametrization is explained. Then, the procedure to quantify penetration is detailed. The formulation of the contact virtual work is presented for a penalty approach.

2.1.1. Parametrization of the surface

The geometrically exact beam (GEB) Simo-Reissner theory [7, 16, 17, 31, 35, 37, 38] is used in this contribution. This entails that the beams are shear-deformable and that rigid cross-sections are considered, which cannot warp.

The surface of beam $\mathcal{B}$ is parameterized with two convective parameters $\underline{h} = [h^1, h^2]^T$. $h^1 \in [0, L]$, denotes the arc-length parameter of the beam's centroid line $\mathbf{x}_{0c} : (0, L) \to \mathbb{R}^3$ while $h^2 \in [0, 2\pi]$ is a circumferential parameter of the perimeter of cross-section $\mathcal{C}$ attached to $\mathbf{x}_{0c}(\underline{h})$ (see [12] and Fig. 1). L denotes the initial length of the beam. The location of a surface point in the undeformed configuration in the global coordinate system, $\mathbf{x}_0$, can be

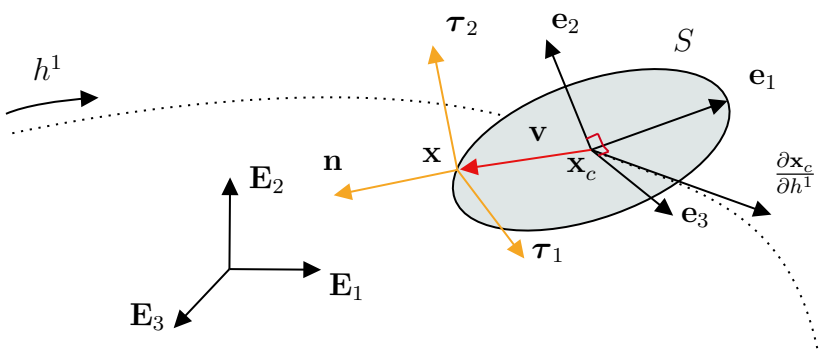

Figure 1: Beam kinematics for current configuration. The beam's centroid-line is presented with a dashed line. Local basis vector $\mathbf{e}_3$ is not aligned with the vector tangent to the centroid-line $\frac{\partial \mathbf{x}_c}{\partial h^1}$ due to shear deformation. A typical vector $\mathbf{v}$ lying on $\mathcal{C}$ (grey ellipse) is presented with a red arrow.

obtained from:

$$\mathbf{x}_0(\underline{h}) = \mathbf{x}_{0c}(h^1) + \mathbf{v}_0(\underline{h}), \tag{1}$$

where $\mathbf{v}_0$ denotes a vector contained in $\mathcal{C}$. Here, we assume that $\mathbf{v}_0$ always connects $\mathbf{x}_{0c}$ to a surface point. In case $\mathcal{C}$ is elliptical, $\mathbf{v}_0$ can be expressed as:

$$\mathbf{v}_0(\underline{h}) = a\cos(h^2)\mathbf{e}_{01}(h^1) + b\sin(h^2)\mathbf{e}_{02}(h^1), \tag{2}$$

where a and b denote the dimensions of the elliptical cross-sections in its principal directions. $\mathbf{e}_{01}$ and $\mathbf{e}_{02}$ are orthonormal basis vectors of the plane containing $\mathcal{C}$. $\mathbf{e}_{03}$ denotes the normal vector to $\mathcal{C}$. The triad $\{\mathbf{e}_{01}, \mathbf{e}_{02}, \mathbf{e}_{03}\}$ forms an orthonormal basis.

Due to the hypothesis of rigid sections, the location of the same material point in the deformed configuration can similarly be obtained from:

$$\mathbf{x}(\underline{h}) = \varphi(\mathbf{x}_0(\underline{h})) = \mathbf{x}_c(h^1) + \mathbf{v}(\underline{h}), \tag{3}$$

where:

$$\mathbf{x}_c = \mathbf{x}_{0c} + \mathbf{u}, \tag{4}$$

denotes the location of the centroid point in the deformed configuration. $\mathbf{u} : (0, L) \to \mathbb{R}^3$ denotes the centroid-line's displacement. φ denotes the deformation mapping relating the current location of a point to its location in the undeformed configuration such that $\mathbf{x}(\underline{h}) = \varphi(\mathbf{X}(\underline{h}))$. $\mathbf{v}$ is obtained from:

$$\mathbf{v}(\underline{h}) = \boldsymbol{\Lambda}(h^1) \cdot \mathbf{v}_0(\underline{h}) = a\cos(h^2)\mathbf{e}_1 + b\sin(h^2)\mathbf{e}_2, \tag{5}$$

where $\boldsymbol{\Lambda} : (0, L) \to SO(3)$, with $SO(3)$ the rotation group, is a rotation tensor that rotates $\mathbf{e}_{0i}$ to $\mathbf{e}_i$ for $i \in \{1, 2, 3\}$. Because shear deformation can be present, $\mathbf{e}_3$ is not necessarily aligned with the tangent to the centroid-line (see Fig. 1). In such cases, *i.e.*:

$$\mathbf{e}_3 \times \frac{\partial \mathbf{x}_c}{\partial h^1} \neq \mathbf{0}, \tag{6}$$

where $\times$ denotes the cross product.

For further use, we define two (covariant) tangent vectors to the surface of $\mathcal{B}$ at $\mathbf{x}(\underline{h})$, denoted by $\boldsymbol{\tau}_1 = \frac{\partial \mathbf{x}}{\partial h^1}$ and $\boldsymbol{\tau}_2 = \frac{\partial \mathbf{x}}{\partial h^2}$ (see Fig. 1). In general, $\boldsymbol{\tau}_1$ and $\boldsymbol{\tau}_2$ are not orthogonal to each other.

2.1.2. Contact Kinematics

We focus here on a system consisting of two bodies: $\mathcal{B}^{\mathrm{I}}$ denotes the thin inner beam and $\mathcal{B}^{\mathrm{J}}$ denotes the hollow outer beam. We assume here that both $\mathcal{B}^{\mathrm{I}}$ and $\mathcal{B}^{\mathrm{J}}$ are modeled as a GEB with plain and hollow cross-sections, respectively. We denote by $\partial\mathcal{B}^{\mathrm{J}}$ the *interior* surface of $\mathcal{B}^{\mathrm{J}}$.

To quantify the penetration of $\mathcal{B}^{\mathrm{I}}$ with $\partial\mathcal{B}^{\mathrm{J}}$, and to quantify the contact area over which this penetration occurs, we:

1. Seed sections along the centroid-line of $\mathcal{B}^{\mathrm{I}}$ (see Fig. 3),
2. For each seeded section, we solve a projection (local) problem to determine if it penetrates $\partial\mathcal{B}^{\mathrm{J}}$ and if so, by how much. This projection problem yields two surface points: one on the perimeter of the seeded section and one on $\partial\mathcal{B}^{\mathrm{J}}$. These points are used to establish a measure of penetration, which in turn determines the amplitude of the contact forces (if penetration is present).

As $\mathcal{B}^{\mathrm{I}}$ and $\mathcal{B}^{\mathrm{J}}$ have a different role, the proposed framework is a master-slave approach. We call $\mathcal{B}^{\mathrm{I}}$ the slave and $\mathcal{B}^{\mathrm{J}}$ the master [40]. Next, we discuss how to compute if a given section of $\mathcal{B}^{\mathrm{I}}$, denoted by $\mathcal{C}$ with perimeter $\partial\mathcal{C}$, penetrates $\partial\mathcal{B}^{\mathrm{J}}$ and if so, how the amount of penetration is computed.

It must be noted that the proposed contact algorithm can only be used if one contact area occurs for each cross-sections (left in Fig. 2). The contact framework can thus not handle scenarios as presented on the right in Fig. 2. If the cross-sections of $\mathcal{B}^{\mathrm{I}}$ is perfectly aligned with the cross-sections of $\mathcal{B}^{\mathrm{J}}$, only one contact area occurs if:

$$\frac{(a_{inner})^2}{b_{inner}} < \frac{(b_{outer})^2}{a_{outer}} \qquad a_{inner} \geq b_{inner} \qquad a_{outer} \geq b_{outer}, \tag{7}$$

where subscript *inner* refers to the inner beam and subscript *outer* refers to the inner cross-sections of the outer beam.

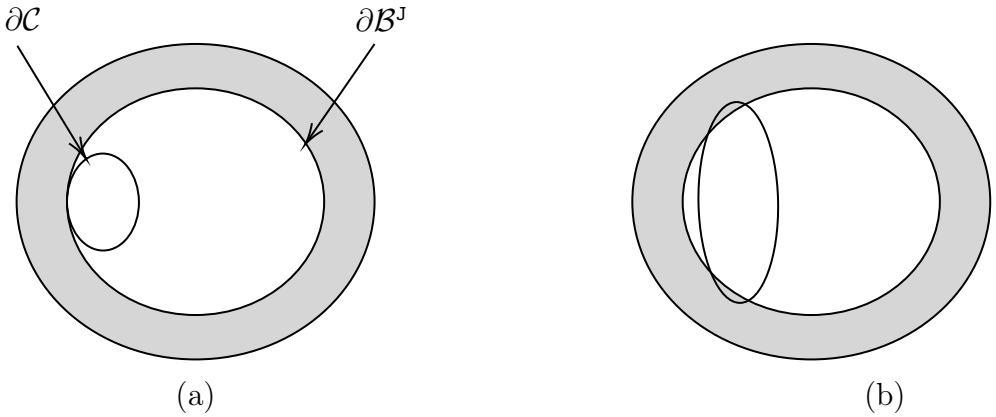

Figure 2: Problem of multiple contact areas: (a) single contact area and (b) two contact areas.

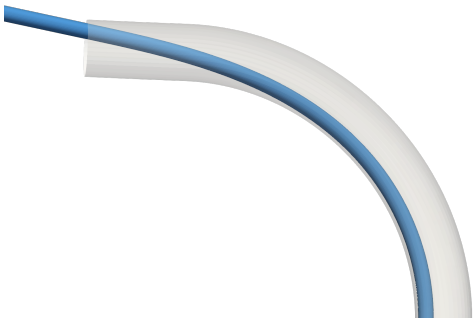

(a) Example of beam-inside-beam contact. The surface of the outer beam is shown in translucent and the one of the inner beam in cyan.

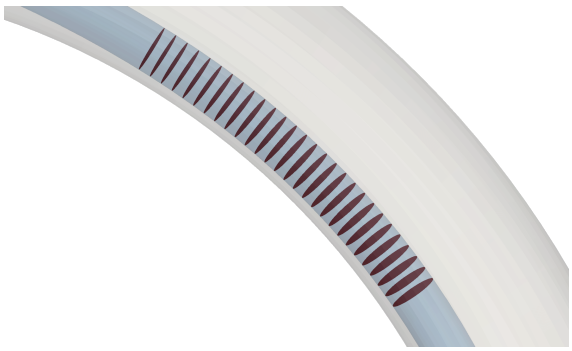

(b) Zoom around the region of contact. The penetrated sections are indicated in red.

Figure 3: (a) Two beams in contact. (b) Sections for which penetration has been detected

We now introduce $\mathbf{n}^{\mathrm{I}}$, an outward pointing unit vector normal to $\partial\mathcal{B}^{\mathrm{I}}$. It is defined as follows:

$$\mathbf{n}^{\mathrm{I}}\left(\underline{h}^{\mathrm{I}}\right) = \frac{\boldsymbol{\tau}_1^{\mathrm{I}}(\underline{h}^{\mathrm{I}}) \times \boldsymbol{\tau}_2^{\mathrm{I}}(\underline{h}^{\mathrm{I}})}{\left\|\boldsymbol{\tau}_1^{\mathrm{I}}(\underline{h}^{\mathrm{I}}) \times \boldsymbol{\tau}_2^{\mathrm{I}}(\underline{h}^{\mathrm{I}})\right\|}. \tag{8}$$

$\mathbf{n}^{\mathrm{J}}$ on the other hand is the *inward* pointing unit vector normal to $\partial\mathcal{B}^{\mathrm{J}}$. It is defined as follows:

$$\mathbf{n}^{\mathrm{J}}\left(\underline{h}^{\mathrm{J}}\right) = \frac{\boldsymbol{\tau}_1^{\mathrm{J}}(\underline{h}^{\mathrm{J}}) \times \boldsymbol{\tau}_2^{\mathrm{J}}(\underline{h}^{\mathrm{J}})}{\left\|\boldsymbol{\tau}_1^{\mathrm{J}}(\underline{h}^{\mathrm{J}}) \times \boldsymbol{\tau}_2^{\mathrm{J}}(\underline{h}^{\mathrm{J}})\right\|}. \tag{9}$$

Local problem and measure of penetration between $\partial\mathcal{C}$ and $\partial\mathcal{B}^{\mathrm{J}}$.
We will now investigate if $\mathcal{C}$, the cross-section uniquely defined by convective coordinate $h^{\mathcal{C}}$, penetrates $\partial\mathcal{B}^{\mathrm{J}}$ and if so, by how much. The so-called gap vector $\mathbf{g}$ connects a point on the perimeter of $\mathcal{C}$, $\mathbf{x}^{\mathrm{I}} \in \partial\mathcal{C}$, to a surface point on $\partial\mathcal{B}^{\mathrm{J}}$, $\mathbf{x}^{\mathrm{J}}$:

$$\mathbf{g}(h^{\mathcal{C}}, h^{\mathrm{I}2}, h^{\mathrm{J}1}, h^{\mathrm{J}2}) = \mathbf{x}^{\mathrm{J}}(h^{\mathrm{J}1}, h^{\mathrm{J}2}) - \mathbf{x}^{\mathrm{I}}(h^{\mathcal{C}}, h^{\mathrm{I}2}). \tag{10}$$

A local (or projection) problem must now be solved, which yields points $\bar{\mathbf{x}}^{\mathrm{I}}$ and $\bar{\mathbf{x}}^{\mathrm{J}}$, such that an appropriate measure of penetration is established. Four convective coordinates are involved in the local problem: $h^{\mathcal{C}}$, which is fixed, as well as $h^{\mathrm{I}2}, h^{\mathrm{J}1}$ and $h^{\mathrm{J}2}$ that are to be determined.

A possibility to determine the unknown convective coordinates would be to solve an optimization problem by minimizing an objective function. Another possibility [12–14, 21, 22, 33] is to solve for a set of equations that does not stem from an objective function, generally unilateral or bilateral orthogonality conditions. Previously, we have shown that the latter makes resolution of the local problem 20-30% faster to solve for beam-to-beam contact [28]. We therefore consider a similar approach for the beam-inside-beam contact of this contribution. Three of the equations we solve for are expressed as:

$$\mathbf{f}_1(\underline{\bar{q}}) = \bar{\mathbf{x}}^{\mathrm{J}} - \bar{\mathbf{x}}^{\mathrm{I}} - \bar{g}\bar{\mathbf{n}}^{\mathrm{I}} = \mathbf{0}, \tag{11}$$

where:

$$\underline{q} = \left[h^{\mathtt{I}2}, h^{\mathtt{I}1}, h^{\mathtt{J}2}, g\right]^T, \tag{12}$$

denotes the array of unknowns. Here and in the following, an overhead bar over a quantity indicates that it is evaluated at the solution of the projection problem. Thus, $\bar{\underline{q}}$ denotes the array solution of Eq. (11). The independent variable $\bar{g}$ quantifies penetration measured in the normal direction, usually denoted as g_N and defined as:

$$g_N = \bar{g} = (\bar{\mathbf{x}}^{\mathtt{J}} - \bar{\mathbf{x}}^{\mathtt{I}}) \cdot \bar{\mathbf{n}}^{\mathtt{I}}. \tag{13}$$

As four variables are present for only three equations, the system of Eq. (11) is underdetermined An additional equation is required. To this end, we introduce plane $\mathcal{P}$ spanned by $\mathbf{n}^{\mathtt{I}}$ and $\boldsymbol{\tau}_2^{\mathtt{I}}$ with the following normal vector:

$$\tilde{\mathbf{n}}^{\mathtt{I}} = \boldsymbol{\tau}_2^{\mathtt{I}} \times \mathbf{n}^{\mathtt{I}}. \tag{14}$$

Also, we define $\mathbf{n}^{\mathtt{J}p}$ as the normalized projection of $\mathbf{n}^{\mathtt{J}}$ on $\mathcal{P}$:

$$\mathbf{n}^{\mathtt{J}p} = \frac{\mathbf{n}^{\mathtt{J}} - (\mathbf{n}^{\mathtt{J}} \cdot \tilde{\mathbf{n}}^{\mathtt{I}})\tilde{\mathbf{n}}^{\mathtt{I}}}{\|\mathbf{n}^{\mathtt{J}} - (\mathbf{n}^{\mathtt{J}} \cdot \tilde{\mathbf{n}}^{\mathtt{I}})\tilde{\mathbf{n}}^{\mathtt{I}}\|}. \tag{15}$$

At the solution of the local problem, we want $\mathbf{n}^{\mathtt{I}}$ and $\mathbf{n}^{\mathtt{J}p}$ to be orthogonal to $\boldsymbol{\tau}_2^{\mathtt{J}}$ (see Fig. 4). This is true if the following equation holds:

$$f_2(\bar{\underline{q}}) = a^{\mathcal{C}}(\mathbf{n}^{\mathtt{I}} + \mathbf{n}^{\mathtt{J}p}) \cdot \boldsymbol{\tau}_2^{\mathtt{J}} = 0, \tag{16}$$

where $a^{\mathcal{C}}$ denotes the dimension of $\mathcal{C}$ along its largest semi-axis which is used to scale $\mathbf{f}_1$ such that $\mathbf{f}_1$ and f_2 have the same units. The set of equations to solve for is now abbreviated as follows:

$$\underline{f}(\bar{\underline{q}}) = \left[\mathbf{f}_1(\bar{\underline{q}}), f_2(\bar{\underline{q}})\right]^T = \underline{0}. \tag{17}$$

We will further interpret $\bar{g}$ as the amount of penetration and is measured in the direction of $\mathbf{n}^{\mathtt{I}}(h^{\mathcal{C}}, \bar{h}^{\mathtt{I}2})$. The set of equations to solve for in Eq. (17) is nonlinear. To solve it, we apply Newton's method for which we linearise residual $\underline{f}$ which requires the following Jacobian:

$$\underline{\underline{H}}(\underline{q}) \;=\; \frac{\partial \underline{f}}{\partial \underline{q}} = \begin{bmatrix} \frac{\partial \mathbf{f}_1}{\partial \underline{q}} \\ \left(\frac{\partial f_2}{\partial \underline{q}}\right)^T \end{bmatrix}. \tag{18}$$

To compute the components of $\underline{\underline{H}}$, we need to introduce the following quantities:

1. Contravariant components $M^{\mathcal{K}ij}$ of $\boldsymbol{M}^{\mathcal{K}}$, the metric tensor of the surface of body $\mathcal{K}$, read:
$$\begin{bmatrix} M^{\mathcal{K}11} & M^{\mathcal{K}12} \\ M^{\mathcal{K}21} & M^{\mathcal{K}22} \end{bmatrix} = \begin{bmatrix} M^{\mathcal{K}}_{11} & M^{\mathcal{K}}_{12} \\ M^{\mathcal{K}}_{21} & M^{\mathcal{K}}_{22} \end{bmatrix}^{-1} = \begin{bmatrix} \boldsymbol{\tau}^{\mathcal{K}}_1 \cdot \boldsymbol{\tau}^{\mathcal{K}}_1 & \boldsymbol{\tau}^{\mathcal{K}}_1 \cdot \boldsymbol{\tau}^{\mathcal{K}}_2 \\ \boldsymbol{\tau}^{\mathcal{K}}_2 \cdot \boldsymbol{\tau}^{\mathcal{K}}_1 & \boldsymbol{\tau}^{\mathcal{K}}_2 \cdot \boldsymbol{\tau}^{\mathcal{K}}_2 \end{bmatrix}^{-1}. \tag{19}$$
2. The second order surface derivatives:
$$\boldsymbol{\tau}^{\mathcal{K}}_{ij} = \frac{\partial \boldsymbol{\tau}^{\mathcal{K}}_i}{\partial h^{\mathcal{K}}_j}. \tag{20}$$

3. The covariant components of curvature tensor $\boldsymbol{C}^{\mathcal{K}}$:

$$C_{ij}^{\mathcal{K}} = \boldsymbol{\tau}_{ij}^{\mathcal{K}} \cdot \mathbf{n}^{\mathcal{K}} \tag{21}$$

4. Weingarten's formula:

$$\frac{\partial \mathbf{n}^{\mathcal{K}}}{\partial h_j} = -M^{\mathcal{K}jk} C_{ki}^{\mathcal{K}} \boldsymbol{\tau}_j^{\mathcal{K}}. \tag{22}$$

Making use of Eq. (22), the partial derivatives of $\mathbf{f}_1$ with respect to $\underline{q}$ in Eq. (18) yield:

$$\frac{\partial \mathbf{f}_1}{\partial \underline{q}} = \left[\frac{\partial \mathbf{f}_1}{\partial h^{\mathtt{I}2}}, \frac{\partial \mathbf{f}_1}{\partial h^{\mathtt{J}1}}, \frac{\partial \mathbf{f}_1}{\partial h^{\mathtt{J}2}}, \frac{\partial \mathbf{f}_1}{\partial g}\right] = \left[\boldsymbol{\tau}_2^{\mathtt{I}} + g\left(M^{\mathtt{I}jk} C_{k2}^{\mathtt{I}} \boldsymbol{\tau}_j^{\mathtt{I}}\right), \boldsymbol{\tau}_1^{\mathtt{J}}, \boldsymbol{\tau}_2^{\mathtt{J}}, -\mathbf{n}^{\mathtt{I}}\right]. \tag{23}$$

The differentiation of f_2 with respect to $\underline{q}$ gives:

$$\frac{\partial f_2}{\partial \underline{q}} = \left[\frac{\partial f_2}{\partial h^{\mathtt{I}2}}, \frac{\partial f_2}{\partial h^{\mathtt{J}1}}, \frac{\partial f_2}{\partial h^{\mathtt{J}2}}, \frac{\partial f_2}{\partial g}\right]^T. \tag{24}$$

Corresponding expressions are more complicated, in particular because $\mathbf{n}^{\mathtt{J}p}$ depends on $h^{\mathtt{I}2}, h^{\mathtt{J}1}$ and $h^{\mathtt{J}2}$.

We now rewrite $\mathbf{n}^{\mathtt{J}p}$ as:

$$\mathbf{n}^{\mathtt{J}p} = \frac{\mathbf{N}^{\mathbf{n}^{\mathtt{J}p}}}{l^{\mathbf{n}^{\mathtt{J}p}}}, \tag{25}$$

where:

$$\mathbf{N}^{\mathbf{n}^{\mathtt{J}p}} = \mathbf{n}^{\mathtt{J}} \cdot (\boldsymbol{I} - \tilde{\mathbf{n}}^{\mathtt{I}} \otimes \tilde{\mathbf{n}}^{\mathtt{I}}) = \mathbf{n}^{\mathtt{J}} \cdot \boldsymbol{D}, \tag{26}$$

and:

$$l^{\mathbf{n}^{\mathtt{J}p}} = \left\| \mathbf{N}^{\mathbf{n}^{\mathtt{J}\mathtt{p}}} \right\|. \tag{27}$$

The partial derivative of $\mathbf{n}^{\mathtt{J}p}$ with respect to the k^{th}-surface parameter of body $\mathtt{1}$ reads:

$$\frac{\partial \mathbf{n}^{\mathtt{J}p}}{\partial h^{\mathtt{1}k}} = \frac{1}{l^{\mathbf{n}^{\mathtt{J}p}}} \left(\mathbf{I} - \mathbf{n}^{\mathtt{J}\mathtt{p}} \otimes \mathbf{n}^{\mathtt{J}\mathtt{p}}\right) \cdot \frac{\partial \mathbf{N}^{\mathbf{n}^{\mathtt{J}\mathtt{p}}}}{\partial h^{\mathtt{1}k}} = \boldsymbol{E} \cdot \frac{\partial \mathbf{N}^{\mathbf{n}^{\mathtt{J}\mathtt{p}}}}{\partial h^{\mathtt{1}k}}, \tag{28}$$

where:

$$\begin{aligned}
\frac{\partial \mathbf{N}^{\mathbf{n}^{\mathtt{J}\mathtt{p}}}}{\partial h^{\mathtt{1}k}} &= \frac{\partial \mathbf{n}^{\mathtt{J}}}{\partial h^{\mathtt{1}k}} \cdot \boldsymbol{D} - \mathbf{n}^{\mathtt{J}} \cdot \frac{\partial \boldsymbol{D}}{\partial h^{\mathtt{1}k}} \\
&= \frac{\partial \mathbf{n}^{\mathtt{J}}}{\partial h^{\mathtt{1}k}} \cdot \boldsymbol{D} - \mathbf{n}^{\mathtt{J}} \cdot \left(\frac{\partial \tilde{\mathbf{n}}^{\mathtt{I}}}{\partial h^{\mathtt{1}k}} \otimes \tilde{\mathbf{n}}^{\mathtt{I}} + \tilde{\mathbf{n}}^{\mathtt{I}} \otimes \frac{\partial \tilde{\mathbf{n}}^{\mathtt{I}}}{\partial h^{\mathtt{1}k}}\right) \qquad (29) \\
&= \delta^{l\mathtt{J}} \left(-M^{\mathtt{J}lm} C_{mk} \boldsymbol{\tau}_{\mathcal{K}}\right) \cdot \boldsymbol{D} - \mathbf{n}^{\mathtt{J}} \cdot \left(\frac{\partial \tilde{\mathbf{n}}^{\mathtt{I}}}{\partial h^{\mathtt{1}k}} \otimes \tilde{\mathbf{n}}^{\mathtt{I}} + \tilde{\mathbf{n}}^{\mathtt{I}} \otimes \frac{\partial \tilde{\mathbf{n}}^{\mathtt{I}}}{\partial h^{\mathtt{1}k}}\right), \qquad (30)
\end{aligned}$$

where δ denotes the Kronecker symbol (not to be confused with the variation symbol). The term $\frac{\partial \tilde{\mathbf{n}}^{\mathtt{I}}}{\partial h^{\mathtt{1}k}}$, where:

$$\tilde{\mathbf{n}}^{\mathtt{I}} = \frac{\mathbf{N}^{\tilde{\mathbf{n}}^{\mathtt{J}}}}{l^{\mathbf{N}^{\tilde{\mathbf{n}}^{\mathtt{J}}}}}, \tag{31}$$

with:

$$\mathbf{N}^{\tilde{\mathbf{n}}^{\mathtt{J}}} = \boldsymbol{\tau}_2^{\mathtt{I}} \times \mathbf{n}^{\mathtt{I}}, \tag{32}$$

and:

$$l^{\mathbf{N}^{\tilde{\mathbf{n}}^{\mathrm{J}}}} = \left\| \boldsymbol{\tau}_2^{\mathrm{I}} \times \mathbf{n}^{\mathrm{I}} \right\|, \tag{33}$$

reads:

$$\frac{\partial \tilde{\mathbf{n}}^{\mathrm{I}}}{\partial h^{1k}} = \frac{1}{l^{\mathbf{N}^{\tilde{\mathbf{n}}^{\mathrm{J}}}}} \left(\mathbf{I} - \tilde{\mathbf{n}}^{\mathrm{I}} \otimes \tilde{\mathbf{n}}^{\mathrm{I}} \right) \cdot \frac{\partial \mathbf{N}^{\tilde{\mathbf{n}}^{\mathrm{J}}}}{\partial h^{1k}} = \boldsymbol{F} \cdot \frac{\partial \mathbf{N}^{\tilde{\mathbf{n}}^{\mathrm{J}}}}{\partial h^{1k}}. \tag{34}$$

We can write:

$$\frac{\partial \mathbf{N}^{\tilde{\mathbf{n}}^{\mathrm{J}}}}{\partial h^{1k}} = \delta^{1\mathrm{I}} \left(\boldsymbol{\tau}_{2k}^{\mathrm{I}} \times \mathbf{n}^{\mathrm{I}} + \boldsymbol{\tau}_2^{\mathrm{I}} \times \left(-M^{\mathrm{I}ij} C_{jk}^{\mathrm{I}} \boldsymbol{\tau}_i^{\mathrm{I}} \right) \right) = \mathbf{c}, \tag{35}$$

such that:

$$\frac{\partial \tilde{\mathbf{n}}^{\mathrm{I}}}{\partial h^{1k}} = \boldsymbol{F} \cdot \mathbf{c}. \tag{36}$$

Finally, this yields:

$$\begin{aligned} \frac{\partial \mathbf{n}^{\mathrm{J}p}}{\partial h^{1k}} =& \frac{1}{l^{\mathbf{n}^{\mathrm{J}p}}} \left(\mathbf{I} - \mathbf{n}^{\mathrm{J}\mathbf{p}} \otimes \mathbf{n}^{\mathrm{J}\mathbf{p}} \right) \cdot \frac{\partial \mathbf{N}^{\mathbf{n}^{\mathrm{J}\mathbf{p}}}}{\partial h^{\mathrm{I}2}} \\ =& \boldsymbol{E} \cdot \left(\delta^{l\mathrm{J}} \left(-M^{\mathrm{J}lm} C_{mk} \boldsymbol{\tau}_{\mathcal{K}} \right) \cdot \boldsymbol{D} - \mathbf{n}^{\mathrm{J}} \cdot \left((\boldsymbol{F} \cdot \mathbf{c}) \otimes \tilde{\mathbf{n}}^{\mathrm{I}} + \tilde{\mathbf{n}}^{\mathrm{I}} \otimes (\boldsymbol{F} \cdot \mathbf{c}) \right) \right) \\ =& \mathbf{d}^{1k}. \end{aligned} \tag{37}$$

Using Eq. (37), compact expressions for the components of $\frac{\partial f_2}{\partial \underline{q}}$ in Eq. (24) can be obtained:

$$\begin{aligned} \frac{\partial f_2}{\partial h^{\mathrm{I}2}} &= a^{\mathcal{C}} \left(\frac{\partial \mathbf{n}^{\mathrm{I}}}{\partial h^{\mathrm{I}2}} + \frac{\partial \mathbf{n}^{\mathrm{J}p}}{\partial h^{\mathrm{I}2}} \right) \cdot \boldsymbol{\tau}_2^{\mathrm{J}} \\ &= a^{\mathcal{C}} \left(-M^{\mathrm{I}jk} C_{k2}^{\mathrm{I}} \boldsymbol{\tau}_j^{\mathrm{I}} + \mathbf{d}^{\mathrm{I}2} \right) \cdot \boldsymbol{\tau}_2^{\mathrm{J}}, \end{aligned} \tag{38}$$

$$\begin{aligned} \frac{\partial f_2}{\partial h^{\mathrm{J}1}} =& a^{\mathcal{C}} \left(\frac{\partial \mathbf{n}^{\mathrm{J}p}}{\partial h^{\mathrm{J}1}} \cdot \boldsymbol{\tau}_2^{\mathrm{J}} + \mathbf{n}^{\mathrm{J}p} \cdot \frac{\partial \boldsymbol{\tau}_2^{\mathrm{J}}}{\partial h^{\mathrm{J}1}} \right) \\ =& a^{\mathcal{C}} \left(\mathbf{d}^{\mathrm{J}1} \cdot \boldsymbol{\tau}_2^{\mathrm{J}} + \mathbf{n}^{\mathrm{J}p} \cdot \boldsymbol{\tau}_{21}^{\mathrm{J}} \right), \end{aligned} \tag{39}$$

$$\begin{aligned} \frac{\partial f_2}{\partial h^{\mathrm{J}2}} &= a^{\mathcal{C}} \left(\frac{\partial \mathbf{n}^{\mathrm{J}p}}{\partial h^{\mathrm{J}2}} \cdot \boldsymbol{\tau}_2^{\mathrm{J}} + \mathbf{n}^{\mathrm{J}p} \cdot \frac{\partial \boldsymbol{\tau}_2^{\mathrm{J}}}{\partial h^{\mathrm{I}2}} \right) \\ &= a^{\mathcal{C}} \left(\mathbf{d}^{\mathrm{J}2} \cdot \boldsymbol{\tau}_2^{\mathrm{J}} + \mathbf{n}^{\mathrm{J}p} \cdot \boldsymbol{\tau}_{22}^{\mathrm{J}} \right). \end{aligned} \tag{40}$$

Combining Eqs. (23), (38), (39), (40), $\underline{\underline{H}}$ reads:

$$\underline{\underline{H}} = \begin{bmatrix} \boldsymbol{\tau}_2^{\mathrm{I}} + g \left(M^{\mathrm{I}jk} C_{k2}^{\mathrm{I}} \boldsymbol{\tau}_j^{\mathrm{I}} \right) & \boldsymbol{\tau}_1^{\mathrm{J}} & \boldsymbol{\tau}_2^{\mathrm{J}} & -\mathbf{n}^{\mathrm{I}} \\ a^{\mathcal{C}} \left(-M^{\mathrm{I}jk} C_{k2}^{\mathrm{I}} \boldsymbol{\tau}_j^{\mathrm{I}} + \mathbf{d}^{\mathrm{I}2} \right) \cdot \boldsymbol{\tau}_2^{\mathrm{J}} & a^{\mathcal{C}} \left(\mathbf{d}^{\mathrm{J}1} \cdot \boldsymbol{\tau}_2^{\mathrm{J}} + \mathbf{n}^{\mathrm{J}p} \cdot \boldsymbol{\tau}_{21}^{\mathrm{J}} \right) & a^{\mathcal{C}} \left(\mathbf{d}^{\mathrm{J}2} \cdot \boldsymbol{\tau}_2^{\mathrm{J}} + \mathbf{n}^{\mathrm{J}p} \cdot \boldsymbol{\tau}_{22}^{\mathrm{J}} \right) & 0 \end{bmatrix}. \tag{41}$$

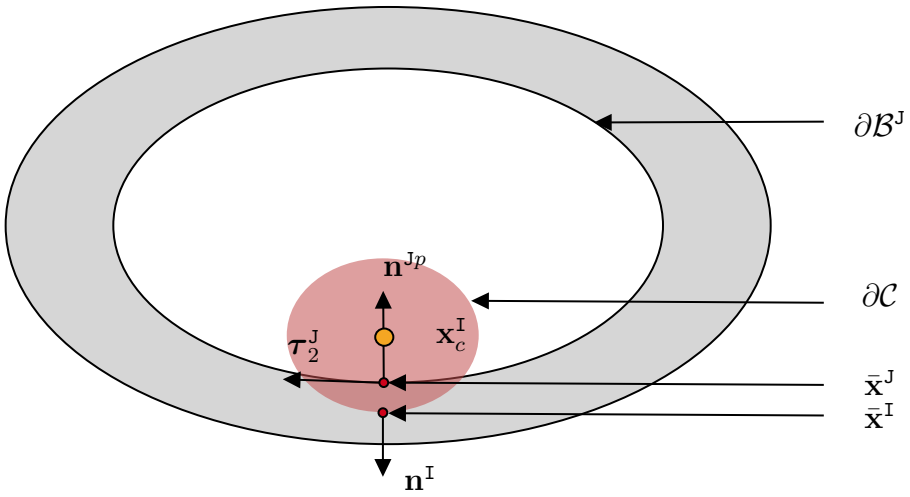

(a)

Figure 4: Perpendicular view to the plane $\mathcal{P}$ of $\partial\mathcal{C}$. Surface points $\bar{\mathbf{x}}^{\mathrm{I}}$ and $\bar{\mathbf{x}}^{\mathrm{J}}$, obtained after solving Eq. (17), are presented as red dots. Vectors $\mathbf{n}^{\mathrm{I}}$ and $\mathbf{n}^{\mathrm{J}p}$ are both orthogonal to $\boldsymbol{\tau}_2^{\mathrm{J}}$.

First-guess procedure.
As stated above, Eq. (17) is solved iteratively. An initial guess of the local parameters $\underline{q}$ must be provided to the solver employed to solve it. We employ a simple two-step procedure to establish an appropriate first guess:

1. We (approximately) find the centroid point of the master body that is the closest to the centroid point of the slave cross-section, $\mathbf{x}_c^{\mathrm{I}}(h^{\mathcal{C}})$. A simple way of achieving this is by sampling cross-section points along the master beam's centroid-line and pick the closest centroid-point from $\mathbf{x}_c^{\mathrm{I}}(h^{\mathcal{C}})$. The associated convective parameter of the closest sampled centroid point is denoted by $h^{\mathrm{J}1,fg}$.
2. To determine the initial values of circumferential parameters $h^{\mathrm{I}2,fg}$ and $h^{\mathrm{J}2,fg}$, we locate a pair of perimeter points on the cross-sections attached to $\mathbf{x}_c^{\mathrm{I}}(h^{\mathcal{C}})$ and $\mathbf{x}_c^{\mathrm{J}}(h^{\mathrm{J}1,fg})$. This procedure is depicted in Fig. 5. We start by sampling four points on the perimeter of both cross-sections. The pair of closest points is then chosen. Next, for each cross-section, we seed a point on the middle of each sub-curve attached to the point previously selected ((c) in Fig. 5). Again, the closest pair of points is selected. This procedure is repeated several times. In our simulations, it was repeated until the relative change of the distance between the pair of closest points falls below 10%.

Note that in practice, the approach to establish the initial guess is only performed for a given slave cross-section if it is not active but close to the master surface. If a slave cross-section is active (meaning that it already penetrated the master surface in a previous contact detection), the solution of the local problem of the previous contact detection ($\bar{\underline{q}}$) are used as the first guess.

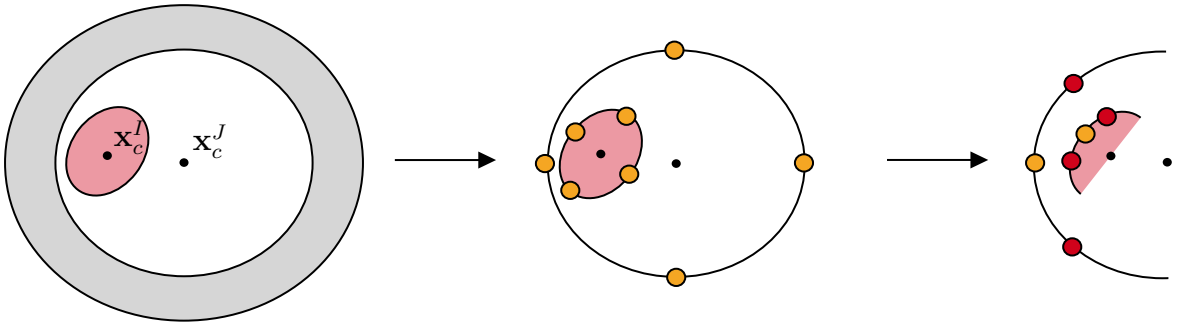

Figure 5: Illustration of the procedure to determine a good initial guess for the local problem. (a) Determination of centroid point $\mathbf{x}_c^{\mathtt{J}}(h^{\mathtt{J}1,fg})$ that must be as close as possible to $\mathbf{x}_c^{\mathtt{I}}(h^{\mathcal{C}})$; (b) Determination of the closest pair of points amongst sampled points on $\partial\mathcal{C}$ and the perimeters of the cross-section attached to $\mathbf{x}_c^{\mathtt{J}}(h^{\mathtt{J}1,fg})$; (c) Determination of the closest pair of points amongst the closest pair of points from (b) (in orange) and points in the middle of the curve connected to theses points (in red).

2.1.3. Contact constraints and virtual work equation including contact

The impenetrability of $\partial\mathcal{C}$ and $\partial\mathcal{B}^{\mathtt{J}}$ is enforced via unilateral contact conditions:

$$g_N \geq 0 \qquad T_N < 0 \qquad g_N T_N = 0, \tag{42}$$

where T_N denotes the nominal contact traction, meaning that it refers to the reference surface area.

In case of contact, a contact virtual work, $\delta\Pi_c$, is added to the virtual work equation for the two-body system and the space of admissible variations $\mathscr{V}$ is modified [40]. In the quasi-static setting, the virtual work reads:

$$\delta\Pi(\underline{p}^{\mathtt{IJ}}, \delta\underline{p}^{\mathtt{IJ}}) = \delta\Pi_{\mathcal{B}^{\mathtt{I}}}(\underline{p}^{\mathtt{I}}, \delta\underline{p}^{\mathtt{I}}) + \delta\Pi_{\mathcal{B}^{\mathtt{J}}}(\underline{p}^{\mathtt{J}}, \delta\underline{p}^{\mathtt{J}}) + \delta\Pi_c(\underline{p}^{\mathtt{IJ}}, \delta\underline{p}^{\mathtt{IJ}}) = 0, \ \forall \delta\underline{p}^{\mathtt{IJ}} \in \mathscr{V}, \tag{43}$$

where $\delta\Pi_{\mathcal{B}^i}$ denotes the internal and external virtual work of beam $\mathcal{B}^i$ (excluding contact interactions). Kinematic variables associated with $\mathcal{B}^i$ are denoted by $\underline{p}^i = \left[\mathbf{u}^i, \boldsymbol{\theta}^i\right]^T : (0, L) \to \mathbb{R}^3 \times \mathbb{R}^3$ and the associated test functions by $\delta\underline{p}^i$. $\mathbf{u}^i$ denotes the displacement field of the $\mathcal{B}^i$'s centroid-line and $\boldsymbol{\theta}^i$ its field of rotation vectors parametrizing SO(3) [16]. $\underline{p}^i$ is only admissible if $\underline{p}^i(\mathbf{X}^{\mathcal{B}^i}) = \underline{p}^i_D(\mathbf{X}^{\mathcal{B}^i}),\ \forall\, \mathbf{X}^{\mathcal{B}^i} \in \partial\mathcal{B}^i_D$. $\partial\mathcal{B}^i_D$ denotes the part of the boundary of $\partial\mathcal{B}^i$ where Dirichlet boundary conditions are imposed [40].

$\underline{p}^{\mathtt{IJ}} = \left[\underline{p}^{\mathtt{I}}, \underline{p}^{\mathtt{J}}\right]^T$ gathers the kinematic variables of both beams. Similarly, test functions are gathered in $\delta\underline{p}^{\mathtt{IJ}} = \left[\delta\underline{p}^{\mathtt{I}}, \delta\underline{p}^{\mathtt{J}}\right]^T$.

In Eq. (43), the virtual work due to contact, $\delta\Pi_c$, accounts for all the sections penetrated. The infinitesimal virtual work produced at a single section, denoted by $d\delta\Pi_c$, can be written as [28]:

$$d\delta\Pi_c = T_N \delta g_N \left\| \frac{\partial \mathbf{x}^{\mathtt{I}}_{0c}}{\partial h^{\mathtt{I}1}} \right\| dh^{\mathtt{I}1}, \tag{44}$$

where δg_N denotes the variation of g_N that depends on all kinematic variables in $\underline{p}^{\mathrm{IJ}}$, and dh^{I1} denotes the differential of the slave's centroid line parameter associated to $\mathcal{C}$. dh^{I1} is related to the differential length of the undeformed centroid-line according to:

$$dL^{\mathcal{B}^{\mathrm{I}}} = \left\| \frac{\partial \mathbf{x}_{0c}^{\mathrm{I}}}{\partial h^{\mathrm{I1}}} \right\| dh^{\mathrm{I1}}, \tag{45}$$

Next, we discuss how to calculate T_N for the penalty approach used in this contribution and also how to compute δg_N. The nominal traction vector has been preferred over the current traction vector as the former must be integrated in the length of the slave beam in the reference configuration, while the latter has to be integrated over the current configuration. As the reference configuration does not depend on $\underline{p}^{\mathrm{IJ}}$, the linearization of $\delta\Pi$ yields shorter expressions than if the current traction vector was employed [26].

Penalty method.
If a penalty formulation is used, contact traction T_N, acting at the pair of surface points $\bar{\mathbf{x}}^{\mathrm{J}}$ and $\bar{\mathbf{x}}^{\mathrm{I}}$, is given by:

$$T_N = -\epsilon_N \langle -g_N \rangle , \tag{46}$$

where $\epsilon_N > 0$ denotes the penalty stiffness and $\langle \bullet \rangle$ denote the Macaulay brackets, representing the positive part of its operand [25]. The fact that ϵ_N must be selected can be seen as a weakness of the penalty method. Indeed, other constraint enforcement methods like the Lagrange multipliers method do not need such user-defined parameters. On the other hand, in the context of contact frameworks for beams that are characterized by rigid cross sections, the penalty parameter can be interpreted as some compliance of the beams in the transversal directions [28, 33]. Inserting Eq. (46) into Eq. (44), the virtual work of the contact force reads:

$$d\delta\Pi_c = -\epsilon_N \langle -g_N \rangle \, \delta g_N \left\| \frac{\partial \mathbf{x}_{0c}^{\mathrm{I}}}{\partial h^{\mathrm{I1}}} \right\| dh^{\mathrm{I1}}. \tag{47}$$

The virtual work of all penetrated sections follows from the integration of the infinitesimal virtual work of a single penetrated section, $d\delta\Pi_c$, along the centroid-line of $\mathcal{B}^{\mathrm{I}}$ as follows:

$$\delta\Pi_c = \int_{h_L^{\mathrm{1I}}}^{h_U^{\mathrm{1I}}} d\delta\Pi_c, \tag{48}$$

where h_L^{1I} and h_U^{1I} are the lower and upper bounds of the integral, respectively.

Variation of the normal gap, δg_N.
$g_N = \bar{\mathbf{g}} \cdot \bar{\mathbf{n}}^{\mathrm{I}}$, measured for a fixed h^{I1}, depends on $\underline{p}^{\mathrm{IJ}}$ but also on the local variables in $\underline{q}$, which in turn implicitly depend on $\underline{p}^{\mathrm{IJ}}$. Eventually, δg_N must be solely expressed in terms of the variations of the primary variables, here $\delta\underline{p}^{\mathrm{IJ}}$. The variational operator applied to g_N gives:

$$\delta g_N = \delta\bar{\mathbf{g}} \cdot \bar{\mathbf{n}}^{\mathrm{I}} + \bar{\mathbf{g}} \cdot \delta\bar{\mathbf{n}}^{\mathrm{I}}. \tag{49}$$

Also, we have:

$$\bar{\mathbf{g}} \cdot \delta\bar{\mathbf{n}}^{\mathrm{I}} = g_N \bar{\mathbf{n}}^{\mathrm{I}} \cdot \delta\bar{\mathbf{n}}^{\mathrm{I}} = 0, \tag{50}$$

as $\delta\bar{\mathbf{n}}^{\mathrm{I}} \cdot \bar{\mathbf{n}}^{\mathrm{I}} = 0$. Noting that $\bar{\mathbf{g}}$ depends on $\underline{p}^{\mathrm{IJ}}$ and $\underline{\bar{q}}(\underline{p}^{\mathrm{IJ}})$, we get:

$$\delta\bar{\mathbf{g}} = \left(\frac{\partial \mathbf{g}}{\partial \underline{p}^{\mathrm{IJ}}}\Big|_{\underline{q}=\underline{\bar{q}}}\right)^T \delta\underline{p}^{\mathrm{IJ}} + \left(\frac{\partial \mathbf{g}}{\partial \underline{q}}\Big|_{\underline{q}=\underline{\bar{q}}}\right)^T \delta\underline{q} \tag{51}$$

$$= \left(\frac{\partial \mathbf{g}}{\partial \underline{p}^{\mathrm{IJ}}}\Big|_{\underline{q}=\underline{\bar{q}}}\right)^T \delta\underline{p}^{\mathrm{IJ}} + \left(\frac{\partial \mathbf{g}}{\partial \underline{q}}\Big|_{\underline{q}=\underline{\bar{q}}}\right)^T \left(\frac{d\underline{q}}{d\underline{p}^{\mathrm{IJ}}}\Big|_{\underline{q}=\underline{\bar{q}}}\right) \delta\underline{p}^{\mathrm{IJ}}. \tag{52}$$

The relationships between $\underline{q}$ and $\underline{p}^{\mathrm{IJ}}$ can be found on the basis of the stationarity of $\underline{f}(\underline{p}^{\mathrm{IJ}}, \underline{\bar{q}}(\underline{p}^{\mathrm{IJ}}))$ with respect to $\underline{p}^{\mathrm{IJ}}$:

$$\frac{d\underline{f}}{d\underline{p}^{\mathrm{IJ}}} = (\frac{\partial \underline{f}}{\partial \underline{p}^{\mathrm{IJ}}}\Big|_{\underline{q}=\underline{\bar{q}}})\delta\underline{p}^{\mathrm{IJ}} + (\underbrace{\frac{\partial \underline{f}}{\partial \underline{q}}}_{\underline{\underline{H}}}\Big|_{\underline{q}=\underline{\bar{q}}})\delta\underline{\bar{q}} = \underline{0}, \tag{53}$$

which leads after some rearrangement to:

$$\delta\underline{\bar{q}} = -\left(\underline{\underline{H}}^{-1}\Big|_{\underline{q}=\underline{\bar{q}}} \frac{\partial \underline{f}}{\partial \underline{p}^{\mathrm{IJ}}}\Big|_{\underline{q}=\underline{\bar{q}}}\right) \delta\underline{p}^{\mathrm{IJ}}. \tag{54}$$

For further use, we define $\underline{\underline{A}}$ as follows:

$$\underline{\underline{A}} = -\underline{\underline{H}}^{-1}\Big|_{\underline{q}=\underline{\bar{q}}} \frac{\partial \underline{f}}{\partial \underline{p}^{\mathrm{IJ}}}\Big|_{\underline{q}=\underline{\bar{q}}}. \tag{55}$$

such that:

$$\delta\underline{\bar{q}} = \underline{\underline{A}}\delta\underline{p}^{\mathrm{IJ}}. \tag{56}$$

Inserting this in Eq. (52) yields:

$$\delta\bar{\mathbf{g}} = \left(\left(\frac{\partial \mathbf{g}}{\partial \underline{p}^{\mathrm{IJ}}}\Big|_{\underline{q}=\underline{\bar{q}}}\right)^T + \left(\frac{\partial \mathbf{g}}{\partial \underline{q}}\Big|_{\underline{q}=\underline{\bar{q}}}\right)^T \underline{\underline{A}}\right) \delta\underline{p}^{\mathrm{IJ}}. \tag{57}$$

Inserting this into Eq. (49) yields:

$$\delta g_N = \delta\bar{\mathbf{g}} \cdot \bar{\mathbf{n}}^{\mathrm{I}} = \left(\frac{\partial \bar{\mathbf{g}}}{\partial \underline{p}^{\mathrm{IJ}}}\right)^T \delta\underline{p}^{\mathrm{IJ}} \cdot \bar{\mathbf{n}}^{\mathrm{I}} + \left(\frac{\partial \bar{\mathbf{g}}}{\partial \underline{q}}\right)^T \underline{\underline{A}}\delta\underline{p}^{\mathrm{IJ}} \cdot \bar{\mathbf{n}}^{\mathrm{I}} \tag{58}$$

$$= (\delta\underline{p}^{\mathrm{IJ}})^T \left(\frac{\partial \bar{\mathbf{g}}}{\partial \underline{p}^{\mathrm{IJ}}} \cdot \bar{\mathbf{n}}^{\mathrm{I}} + \underline{\underline{A}}^T \frac{\partial \bar{\mathbf{g}}}{\partial \underline{q}} \cdot \bar{\mathbf{n}}^{\mathrm{I}}\right) \tag{59}$$

$$= (\delta\underline{p}^{\mathrm{IJ}})^T \underline{z}. \tag{60}$$

Note for further use that $\frac{\partial \bar{\mathbf{g}}}{\partial \underline{p}^{\mathtt{IJ}}} \bar{\mathbf{n}}^{\mathtt{I}}$ reads:

$$\frac{\partial \mathbf{g}}{\partial \underline{p}^{\mathtt{IJ}}}\Big|_{\underline{q}=\bar{\underline{q}}} \cdot \bar{\mathbf{n}}^{\mathtt{I}} = \frac{\partial \bar{\mathbf{x}}^{\mathtt{J}}}{\partial \underline{q}}^{T} \cdot \bar{\mathbf{n}}^{\mathtt{I}} - \frac{\partial \bar{\mathbf{x}}^{\mathtt{I}}}{\partial \underline{q}}^{T} \cdot \bar{\mathbf{n}}^{\mathtt{I}} \tag{61}$$

$$= \begin{bmatrix} 0 \\ \boldsymbol{\tau}_1^{\mathtt{J}} \cdot \bar{\mathbf{n}}^{\mathtt{I}} \\ \boldsymbol{\tau}_2^{\mathtt{J}} \cdot \bar{\mathbf{n}}^{\mathtt{I}} \end{bmatrix} - \begin{bmatrix} \boldsymbol{\tau}_1^{\mathtt{I}} \cdot \bar{\mathbf{n}}^{\mathtt{I}} \\ 0 \\ 0 \end{bmatrix} \tag{62}$$

$$= \begin{bmatrix} 0 \\ \boldsymbol{\tau}_1^{\mathtt{J}} \cdot \bar{\mathbf{n}}^{\mathtt{I}} \\ \boldsymbol{\tau}_2^{\mathtt{J}} \cdot \bar{\mathbf{n}}^{\mathtt{I}} \end{bmatrix} - \begin{bmatrix} 0 \\ 0 \\ 0 \end{bmatrix}, \tag{63}$$

where is it obvious from Eq. (63) that $\frac{\partial \bar{\mathbf{x}}^{\mathtt{I}}}{\partial \underline{q}}^{T} \cdot \bar{\mathbf{n}}^{\mathtt{I}}$ is independent of $\underline{q}$.

All in all, we can write:

$$\delta \Pi_c = \int_{h_L^{1\mathtt{I}}}^{h_U^{1\mathtt{I}}} -\epsilon_N \langle -g_N \rangle \, \underline{z}^T \delta \underline{p}^{\mathtt{IJ}} \left\| \frac{\partial \mathbf{x}_{0c}^{\mathtt{I}}}{\partial h^{\mathtt{I}1}} \right\| dh^{\mathtt{I}1}. \tag{64}$$

2.2. Spatial discretization

2.2.1. Interpolation of the beams' surface

The Finite Element Method (FEM) is the discretisation method used in this work. Each beam is now discretized with a set of beam finite elements (BFEs) [16, 37, 38]. The rotation vectors are the primary rotational kinematic variables [16] that are interpolated. For a BFE $\mathcal{E}$, we denote by $\mathbf{X}_c^h(h^1) : \left(0, L^{\mathcal{E}}\right) \to \mathbb{R}^3$ the interpolated position of its centroid-line, where $L^{\mathcal{E}}$ denotes the length of the centroid-line in the undeformed configuration. $\mathbf{u}_c^h(h_1) : \left(0, L^{\mathcal{E}}\right) \to \mathbb{R}^3$ and $\boldsymbol{\theta}^h(h^1) : \left(0, L^{\mathcal{E}}\right) \to \mathbb{R}^3$ denote the interpolated displacement field of the centroid-line and the interpolated field of rotation vectors, respectively. Rodrigues' formula is used to obtain rotation tensor $\boldsymbol{\Lambda}$ from the interpolated rotation vector[1], denoted $\boldsymbol{\theta}^h$. The displacement of node K is denoted by $\hat{\mathbf{u}}_K^{\mathcal{E}}$ and its rotation vector by $\hat{\boldsymbol{\theta}}_K^{\mathcal{E}}$. The kinematic variables of element $\mathcal{E}$ are gathered in:

$$\underline{p}^{\mathcal{E}} = \left[\hat{\mathbf{u}}_1^{\mathcal{E}}, \ldots, \hat{\mathbf{u}}_{n_u}^{\mathcal{E}}, \hat{\boldsymbol{\theta}}_1^{\mathcal{E}}, \ldots, \hat{\boldsymbol{\theta}}_{n_\theta}^{\mathcal{E}} \right]^T, \tag{65}$$

where n_u and n_θ denote the number of nodes used to interpolate the displacement and the rotation vector, respectively. Since the nodal variables of all BFEs of $\mathcal{B}^{\mathtt{I}}$ and $\mathcal{B}^{\mathtt{J}}$ are denoted by $\underline{\hat{p}}$, the associated variations are denoted by $\delta \underline{\hat{p}}$.

2.2.2. Contact residual and stiffness

The discretized form of the virtual work in Eq. (43) leads to a set of nonlinear equations. Newton's method is generally used to iteratively determine the solution $\underline{\hat{p}}^{sol}$ of the virtual

[1]It is well known that the corresponding finite element formulation does not share the strain-invariance property of the underlying geometrically exact theory [18].

work statement. This requires the linearization of Eq. (43) around an estimate of $\hat{\underline{p}}^{sol}$, $\hat{\underline{p}}$, which yields:

$$\delta\Pi(\hat{\underline{p}} + \triangle\hat{\underline{p}}, \delta\hat{\underline{p}}) \simeq \delta\Pi(\hat{\underline{p}}, \delta\hat{\underline{p}}) + \underline{\underline{\triangle\delta\Pi}}(\hat{\underline{p}}, \delta\hat{\underline{p}})\triangle\hat{\underline{p}} = \delta\hat{\underline{p}}^T(\underline{r}_g + \underline{\underline{K}}_g\triangle\hat{\underline{p}}) \simeq 0, \tag{66}$$

where $\underline{r}_g$ and $\underline{\underline{K}}_g$ denote the global residual force and the global stiffness matrix, respectively. $\triangle\hat{\underline{p}}$ denotes an increment of the nodal variables. The global forces read:

$$\underline{r}_g(\hat{\underline{p}}) = \underline{f}_{int}(\hat{\underline{p}}) + \underline{r}_c(\hat{\underline{p}}) - \underline{f}_{ext}(\hat{\underline{p}}), \tag{67}$$

where $\underline{f}_{int}$ denotes the internal force vector stemming from the contribution of all BFEs, and $\underline{f}_{ext}$ the external force vector. $\underline{r}_c$ contains all the contact contributions from all contact elements, where a contact element refers to a seeded section attached at an integration point (see below) along $\mathcal{B}^{\mathtt{I}}$ and its projection on discretized surface $\partial\mathcal{B}^{\mathtt{J}}$.

Assuming here that $\underline{f}_{ext}$ does not depend on $\underline{p}^{\mathtt{IJ}}$, the global stiffness obtained after the linearization of $\underline{r}_g$, can be decomposed as follows:

$$\underline{\underline{K}}_g = \underline{\underline{K}}_{int} + \underline{\underline{K}}_c, \tag{68}$$

where $\underline{\underline{K}}_{int}$ denotes the stiffness matrix of the BFEs, and $\underline{\underline{K}}_c$ denotes the stiffness matrix of all contact elements.

The contact virtual work is the sum of all contact contributions:

$$\delta\Pi_c(\hat{\underline{p}}, \delta\hat{\underline{p}}) = \sum_{e\in\mathtt{S}} \delta\Pi_{c,e}(\hat{\underline{p}}_e, \delta\hat{\underline{p}}_e), \tag{69}$$

where $\mathtt{S}$ denotes the set of active contact elements (*i.e.* those for which $g_N < 0$), and $\delta\Pi_{c,e}$ denotes the contact virtual work associated with contact element e. If no smoothing procedure of the surface is required [26], each contact elements involves two BFEs, one which is part of the discretization $\mathcal{B}^{\mathtt{I}}$, and the other which is part of the discretization of $\mathcal{B}^{\mathtt{J}}$. However, if a smoothing of the beam's surface is performed, each contact element directly depends on several BFEs of $\mathcal{B}^{\mathtt{I}}$ and of $\mathcal{B}^{\mathtt{J}}$. The set of elements of $\mathcal{B}^{\mathtt{I}}$ and $\mathcal{B}^{\mathtt{J}}$ used to construct contact element e are denoted by $\mathcal{M}$ and $\mathcal{N}$, respectively. The involved nodal variables are gathered in array $\hat{\underline{p}}_e = \left[\hat{\underline{p}}^{\mathcal{M}}, \hat{\underline{p}}^{\mathcal{N}}\right]^T$. Similarly, the involved nodal variations are denoted by $\delta\hat{\underline{p}}_e$.

The linearization of $\delta\Pi_c$ reads:

$$\begin{aligned}
\delta\Pi_c(\hat{\underline{p}} + \triangle\hat{\underline{p}}, \delta\hat{\underline{p}}) &= \sum_{e\in\mathtt{S}} \delta\Pi_{c,e}(\hat{\underline{p}}_e + \triangle\hat{\underline{p}}_e, \delta\hat{\underline{p}}_e) \\
&\approx \sum_{e\in\mathtt{S}} \delta\Pi_c(\hat{\underline{p}}_e, \delta\hat{\underline{p}}_e) + \underline{\underline{\triangle\delta\Pi_c}}(\hat{\underline{p}}_e, \delta\hat{\underline{p}}_e)\triangle\hat{\underline{p}}_e \qquad (70) \\
&\approx \sum_{e\in\mathtt{S}} \delta\hat{\underline{p}}_e^T(\underline{r}_{ce} + \underline{\underline{K}}_{ce}\triangle\hat{\underline{p}}_e). \qquad (71)
\end{aligned}$$

Next, we discuss how to construct element contributions $\underline{r}_{ce}$ and $\underline{\underline{K}}_{ce}$ to the global residual (force) vector and the global stiffness matrix, respectively.

Force vector and stiffness of contact element e.
We numerically integrate Eq. (39) with a quadrature (Gauss or Lobato-type). To this end, we place $n_{IP}^{\mathcal{M}}$ integration points of a single subdomain along the centroid-line of $\mathcal{M}$ [21, 33]. This yields:

$$\delta\Pi_c = -\epsilon_N \int_{-1}^{1} \langle -g_N(\eta)\rangle \, \delta g_N(\eta) \, \|\mathcal{J}(\eta)\| \, d\eta \tag{72}$$

$$\approx -\epsilon_N \sum_{k}^{n_{IP}^{\mathcal{M}}} w_k \, \langle -g_N(\eta_k)\rangle \, \delta g_N(\eta_k) \, \|\mathcal{J}(\eta_k)\| \, , \tag{73}$$

$$\approx \sum_{k}^{n_{IP}^{\mathcal{M}}} w_k \, \langle -g_{Nk}\rangle \, \delta g_{Nk} \, \|\mathcal{J}_k\| \, , \tag{74}$$

where $\eta \in [-1, 1]$ denotes the centroid point coordinate in the parameter space and $\mathcal{J} = \frac{\partial \mathbf{x}_{0c}^{\mathtt{I}}}{\partial \eta}$. The weight and coordinates of the k^{th} integration point are denoted by w_k and η_k, respectively. Given the section along $\mathcal{M}$ attached to $\mathbf{x}_c(\eta)$ for which we solve the local problem of Eq. (17), two surface points, $\bar{\mathbf{x}}^{\mathcal{M}}$ and $\bar{\mathbf{x}}^{\mathcal{N}}$, are computed. In Eq. (73), $\underline{r}_{cek}$ is expressed as:

$$\underline{r}_{cek} = -\epsilon_N \, \langle -g_N\rangle \, \frac{dg_N}{d\underline{\hat{p}}_e}. \tag{75}$$

If the Automatic Differentiation (AD) formalism is employed [23, 24], the dependency of the local variables with respect to $\underline{\hat{p}}_e$ as well as relations of Eq. (63) can be directly incorporated as follows:

$$\delta g_N = \delta\bar{\mathbf{g}} \cdot \bar{\mathbf{n}}^{\mathtt{I}} \tag{76}$$

$$= \delta\bar{\mathbf{x}}^{\mathtt{J}} \cdot \bar{\mathbf{n}}^{\mathtt{I}} - \delta\bar{\mathbf{x}}^{\mathtt{I}} \cdot \bar{\mathbf{n}}^{\mathtt{I}} \tag{77}$$

$$= \left(\frac{\hat{\partial}\mathbf{x}^{\mathtt{J}}}{\hat{\partial}\underline{p}^{\mathtt{IJ}}}\Big|_{\frac{\partial \bar{q}}{\partial \bar{p}^{\mathtt{IJ}}} = \underline{\underline{A}}} - \frac{\hat{\partial}\mathbf{x}^{\mathtt{I}}}{\hat{\partial}\underline{p}^{\mathtt{IJ}}}\Big|_{\frac{\partial \bar{q}}{\partial \bar{p}^{\mathtt{IJ}}} = \underline{\underline{0}}} \right) \cdot \bar{\mathbf{n}}^{\mathtt{I}}, \tag{78}$$

where operator $\frac{\hat{\partial}\square}{\hat{\partial}\underline{w}}$ denotes the Automatic Differentiation (AD) of function $\square$ with respect to the variables in $\underline{w}$ ([23, 26]) and the mechanism of AD exceptions is used to overwrite some partial derivatives.

$\underline{\underline{K}}_{cek}$, stemming for the contribution of the k^{th} integration point placed along $h_1^{\mathcal{M}}$, can be obtained using AD as follows:

$$\underline{\underline{K}}_{cek} = \frac{\hat{\partial}\underline{r}_{cek}}{\hat{\partial}\underline{\hat{p}}_e}\Big|_{\frac{\partial \bar{q}}{\partial \bar{\hat{p}}_e} = \underline{\underline{A}}}. \tag{79}$$

$\underline{r}_c$ and $\underline{\underline{K}}_c$, which contain the contributions of all contact elements in set $\mathtt{S}$, are obtained from:

$$\underline{r}_c = \mathop{\mathsf{A}}_{e\in\mathtt{S}} \sum_{k}^{n_{IP}^{\mathcal{M}}} w_k \underline{r}_{cek} = \mathop{\mathsf{A}}_{e\in\mathtt{S}} \underline{r}_{ce}, \tag{80}$$

$$\underline{\underline{K}}_c = \mathop{\mathsf{A}}_{e\in\mathtt{S}} \sum_{k}^{n_{IP}^{\mathcal{M}}} w_k \underline{\underline{K}}_{cek} = \mathop{\mathsf{A}}_{e\in\mathtt{S}} \underline{\underline{K}}_{ce}. \tag{81}$$

where A denotes the finite-element assembly operator. Note that the exception in differentiation in Eq. (81) allows to properly linearise $\underline{r}_{cek}$ such that the exception $\frac{\partial q}{\partial \underline{\bar{p}}^{\mathtt{IJ}}} = \underline{\underline{0}}$ in Eq. (78) is replaced by $\frac{\partial q}{\partial \underline{\bar{p}}^{\mathtt{IJ}}} = \underline{\underline{A}}$ during linearization.

3. Results

In this section, the beam-inside-beam contact scheme is applied to two numerical examples. First, a thin beam is pulled out from another beam in which it is initially inserted. Second, a thin beam is inserted in a curved beam. For these two examples, a single integration point is used to evaluate $\underline{r}_{ce}$ and $\underline{\underline{K}}_{ce}$ in Eqs. (80) and (81), respectively.

In both examples, large relative displacements of the contacting surfaces take place. This implies that for a contact element, if projection point $\bar{\mathbf{x}}^{\mathtt{J}}$ lies on the surface of BFE $\mathcal{M}$, this projection might go off the bound of the surface $\partial\mathcal{M}$. If this happens, projection point $\bar{\mathbf{x}}^{\mathtt{J}}$ should lie on an adjacent element's surface, namely the surface of element $\mathcal{B}^{\mathcal{M}+1}$ or $\mathcal{B}^{\mathcal{M}-1}$. However, as two-node geometrically exact beam elements are employed, gaps and overlaps of the different BFE's surfaces are present if the beam is not initially straight. For this reason, it might be difficult or impossible to define the new location of $\bar{\mathbf{x}}^{\mathtt{J}}$.

To palliate this problem, a dedicated surface smoothing technique was introduced in [29]. The resulting auxiliary surface has C^1-continuity which is convenient for contact treatment. This procedure is used in the following examples.

Due to the discretization of the contact kinematics, a sudden loss of contact near the inlet and outlet of the outer beam may result in loss of convergence. The methodology presented in Appendix A is therefore adopted in the following examples to avoid this complications.

3.1. Example 1: Pull out

In the first example, two elastic beams with the same initial centroid-line form a part of a helix (Fig. 6a). They have the same centroid-line as a parameterized helix. The outer beam is hollow with an elliptical cross-section defined by $a = 22.3$ mm and $b = 17.8$ mm. Its wall thickness is 0.2 mm. Its Young's modulus is $E = 0.15$ MPa [20] and 75 BFEs are employed to discretize it. The thin beam has an elliptical section with semi-axes $a = 3.9$ mm and $b = 3$ mm. It is stiffer than the hollow beam as its Young's modulus is $E = 1.5$ MPa. Its Poisson's ratio is $\nu = 0.3$ and it is discretized with 100 BFEs. A penalty stiffness of 1 N/m is used. The displacements and rotations of both end nodes of the outer beam are restrained. One end of the thin beam is pulled away from the outer beam by 1200 mm in 300 equally spaced increments.

Contact interactions substantially deform the thin beam, (Fig. 6b). As the (prescribed) end node of the thin beam continues to move away from the outer beam, sliding of the contacting surfaces occurs until the final configuration is reached (Fig 6c). As the prescribed beam deforms and moves along the outer beam, the number of penetrated sections changes (Fig. 7). The components of the reaction force and torque at the prescribed end of the thin beam are reported in Fig. 8a and Fig. 8b, respectively.

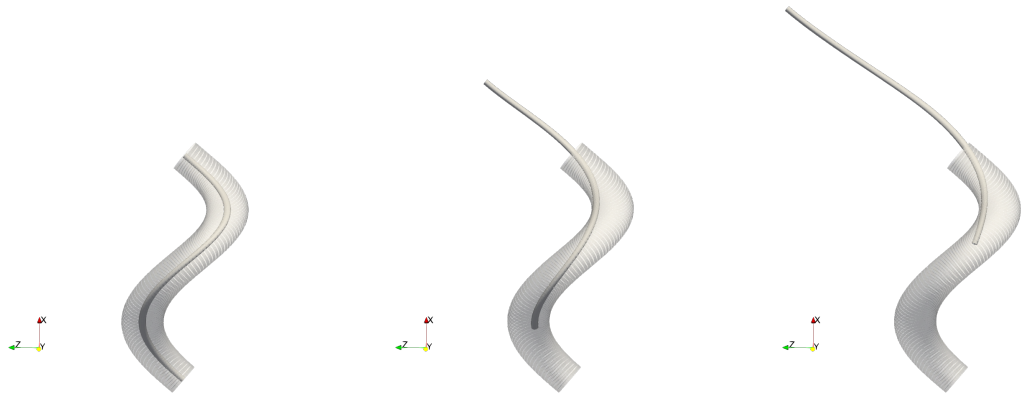

(a) (b) (c)

Figure 6: Example 1: (a) Initial configuration; (b) configuration halfway through the loading, and (c) final configuration.

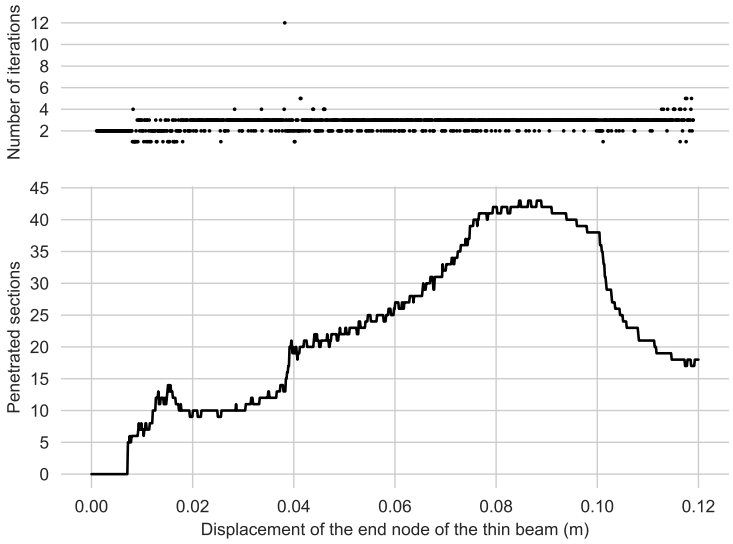

Figure 7: Example 1: top: number of global iterations to reach the convergence criteria $\left\| \underline{f}_{int} + \underline{r}_c - \underline{f}_{ext} \right\| < 10^{-8}$; bottom: number of penetrated sections as a function of the displacement of the end node of the thin beam. The peak in the number of iterations corresponds to the sliding of a cross-section of the slave beam in contact out of the hollow beam. The peak in the number of iterations corresponds to the sliding of a cross-section of the slave beam in contact out of the hollow beam.

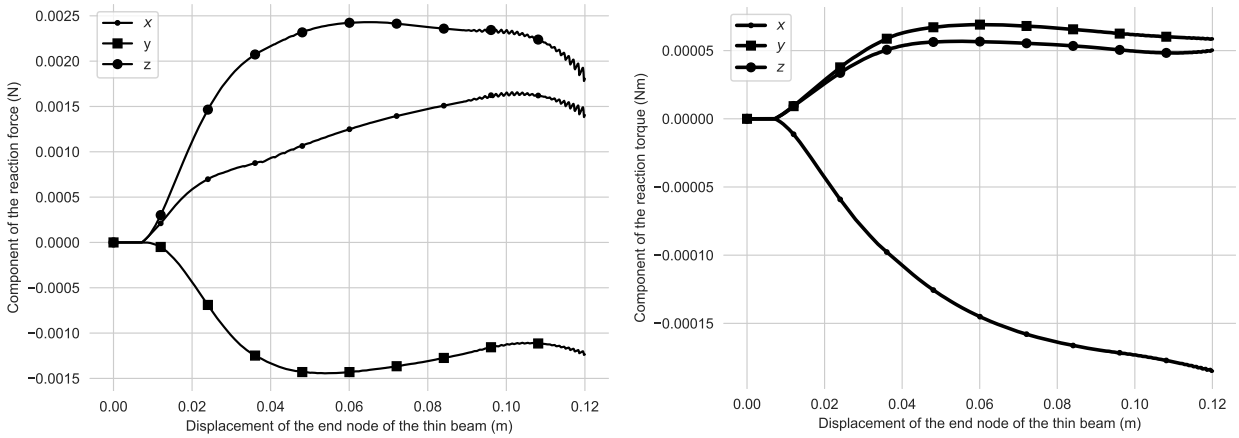

(a) (b)

Figure 8: Example 1: (a) components of the reaction force and (b) reaction torque at the prescribed end of the thin beam.

3.2. Example 2: Insertion

The second example involves an initially straight thin beam that is pushed in a hollow, largely circular beam (see Fig. 9). Initially, only a small part of the thin beam is inserted in the hollow one. The kinematic variables of the outer beam's end node near the thin beam are restrained. The z-displacement of the inner beam's end node furthest away from the outer beam is prescribed to reach 270 mm in 300 increments, whilst the other kinematic variables at this end node are restrained.

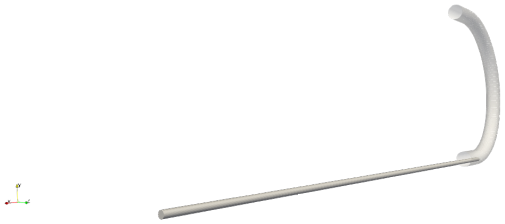

Figure 9: Example 2: Initial configuration.

This inner beam has a length of 54 cm, and a Young's modulus of 1.5 MPa. The cross sectional shapes are given by $a = 5.4\,\text{mm}$ and $b = 4.3\,\text{mm}$. The outer hollow beam is more compliant with $E = 0.15$ MPa. Its wall thickness is 1 mm and its cross-sectional semi-axes are $a = 20\,\text{mm}$ and $b = 16\,\text{mm}$. 100 and 180 BFEs are employed to discretize the inner and outer beam, respectively. The Poisson's ratio of both beams is 0.33.

Both structures deform due to contact, see Fig. 10. Fig. 11 shows that numerous sections of the inner beam penetrate the wall of the outer beam, which indicates that the contact is non-localized. This confirms that in the present case, as well as for the first example, contact cannot be described by a single force acting at the closest pair of surface points. Master-master contact frameworks [12–14, 41, 43] where bi-orthogonality equations must be solved to determine the contact location are difficult to apply in these situations. The reason

(a) (b) (c)

Figure 10: Example 2: (a) Initial configuration; (b) configuration halfway through the loading, and (c) final configuration.

is that they rely on the determination of a minimum of a distance function that is almost constant if surfaces are close to each other on a finite region. The top diagram of Fig. 11, furthermore, shows that only a few iterations are required to reach convergence. This was the same as for the first example, as revealed in the top diagram of Fig. 7. The force-displacement and torque-displacement diagrams of Fig. 12 clearly show that different regimes are present, where each regime is governed by a different number of contact areas.

In the current example, the Young's modulus of the inner beam is ten times larger than that of the outer beam. To demonstrate that the framework is also robust for an entirely different ratio of Young's moduli, the example is repeated with exactly the same geometrical, material and numerical parameters, except for the Young's modulus of the inner beam. Instead of 1.5 MPa, we set the modulus to 150 MPa such that it is thousand times larger than that of the outer beam.

The figures for this additional test case are reported in Appendix B. They show that, although the predicted deformations as well as the force- and torque-curves are completely different (cf. Figs. 10, 11 and 12), the maximum number of iterations is again not more than two.

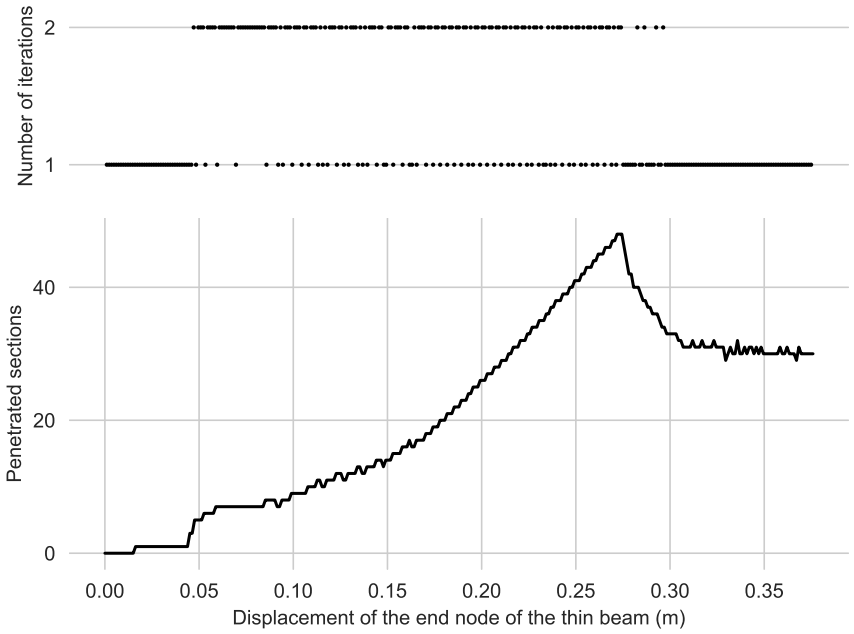

Figure 11: Example 2: Top: number of global iterations to reach convergence criteria: $\left\| \underline{f}_{int} + \underline{r}_c - \underline{f}_{ext} \right\| < 10^{-8}$; Bottom: evolution of the number of contact interactions between sections of the thin beam and the surface of the outer beam.

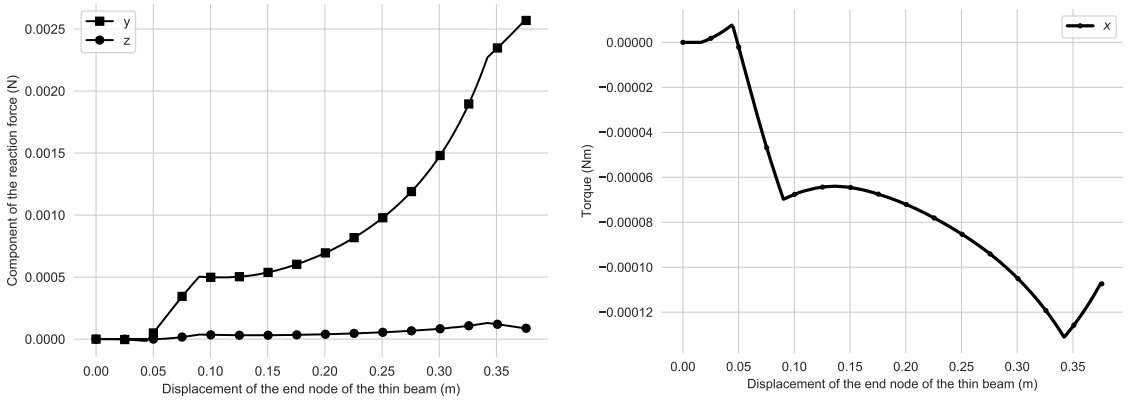

(a) (b)

Figure 12: Example 2: components of the reaction force (a) and torque (b) at the prescribed end of the thin beam.

Mesh convergence study.
The second example is repeated with different meshes in order to show that the results converge to the same solution. For the different meshes, the displacement field of the inner beam is compared to a reference solution, which is obtained with 180 elements for the inner beam. Figs. 13a and 13b show that the displacement fields converge to the reference displacement fields.

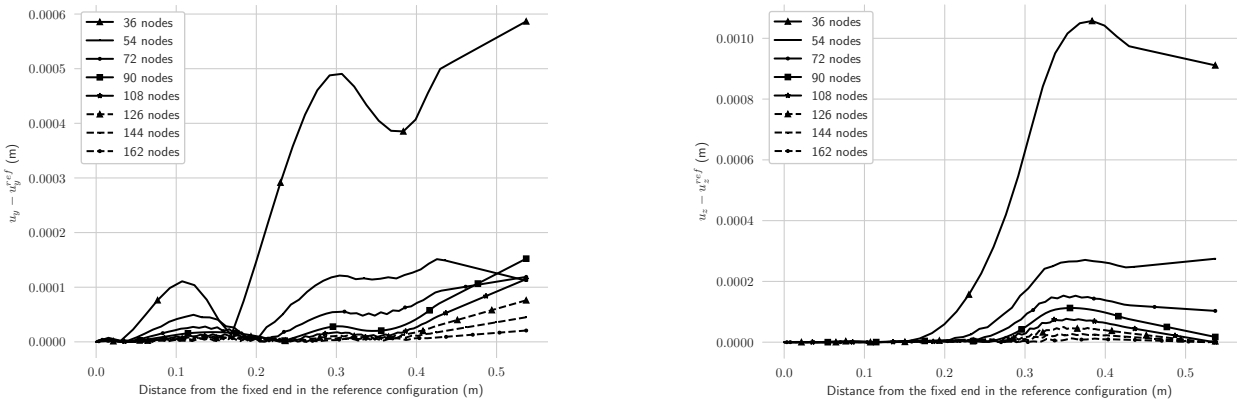

(a) (b)

Figure 13: Effect of the mesh refinement on the final displacement of the nodes of the thin beam. The displacements in the final configuration are compared to the ones with the finest mesh (180 nodes) (a) Difference of the $Y-$displacements ; (b) Difference of the $Z-$displacements.

4. Discussion

The beam-inside-beam contact framework presented in this contribution is the first approach to ensure that an inner beam remains embedded inside an outer, hollow beam because all existing contact frameworks for beams aim to achieve the opposite: they repel beams from each other.

The advantage of using beams over conventional 3D finite elements is the potential to achieve faster simulations (although our particular implementation can surely not compete with frameworks such as SOFA [11]). The disadvantage of using beams over conventional finite elements is a reduction of the simulation accuracy. Hence, the framework proposed in this contribution may be perceived to be beneficial if simulation speed is preferred over simulation accuracy. On the other hand, our framework can handle slender medical instruments with both circular and elliptical cross-sections, whereas the frameworks of [1, 9, 15, 27, 39] have only been demonstrated to handle circular ones. The reason that beams, formulated to rapidly simulate the mechanical behavior of slender bodies, are faster for mechanical simulations involving contact is twofold. First, beams come with fewer degrees of freedom (i.e. kinematic variables) than if the tubes' surfaces are represented by conventional finite elements, because in most beam theories the beams' cross-sections are rigid (*i.e.* the cross-sections cannot deform). Hence, the entire beam's geometry can be constructed from its centroid line description and the cross-sections' orientation. This drastically reduces the number of degrees of freedom necessary to discretise a slender body. Second, and seemingly even more important is the fact that the penetration can be quantified for an entire (rigid) cross-section at once, which drastically reduces the number of local problems that need to be solved.

One possible extension of the beam-inside-beam contact framework is the incorporation of fluid flows inside the hollow beam to represent blood flow. Frictional sliding between the inner and outer beam also seems like a necessary extension for the future. Surrounding tissues were furthermore neglected in the presented simulations, which did not focus on a particular type of intervention in order to highlight the generality of the framework.

The accuracy of the framework is not as high as that of the frameworks presented in [9, 19, 27, 39]. However, simulation speed and simulation accuracy are two competing interests and if speed is preferred over accuracy, our new framework is a promising alternative to existing frameworks.

Acknowledgments

Marco Magliulo, Andreas Zilian and Lars Beex would like to acknowledge the financial support of the University of Luxembourg for project TEXTOOL. Jakub Lengiewicz gratefully acknowledges the financial support of EU Horizon 2020 Marie Sklodowska Curie Individual Fellowship *MOrPhEM* (H2020-MSCA-IF-2017, project no. 800150). This work was partially prepared in the framework of the DRIVEN project funded by the European Union's Horizon 2020 research and innovation programme under grant agreement No. 811099.

Appendix A Treatment of contact at the ends of the outer beam.

In the numerical examples of Section 3, the section at the tip of the inner beam slides along the wall of the outer beam until it exits the outer beam (first two images in Fig. 14). The occurrence of this is monitored, because when it occurs, the contact constraint between the section attached to the last integration point of the inner beam and the outer beam must be deactivated and the increment repeated. Then, no contact interactions to embed the inner beam inside the outer beam may be left. If this is the case, a sudden release of the inner beam may occur which makes the simulation diverge (bottom left in Fig. 14).

To avoid this, an additional constraint is added to the outlet of the hollow beam. It enforces the section at the edge of the outer beam to be in contact with the surface of the inner beam (bottom right in Fig. 14). The local problem to that must be solved to quantify penetration is again given by Eq. (17), except that this time $\mathcal{B}^{\mathtt{I}}$ denotes the outer beam and $\mathcal{B}^{\mathtt{J}}$ the inner one. The method of Lagrange multipliers is used to enforce this constraint. The reason is that if the penalty method is employed and the section at the end of the outer beam is detached from the surface of the inner beam, even with the constraint just added, no penetration is detected and the sudden release of the inner tube would not be avoided.

Ideally, a contact at the closest pair of surface points [12, 13] should be applied at the tip of the inner beam in Fig. 14. In this case, the treatment discussed in this session would not be required. However, this necessitates a framework able to automatically decide which type of contact element to use, as in the ABC formulation of Meier et al. [32]. The development of such a framework for shear-deformable beams with elliptical cross-sections remains for future work.

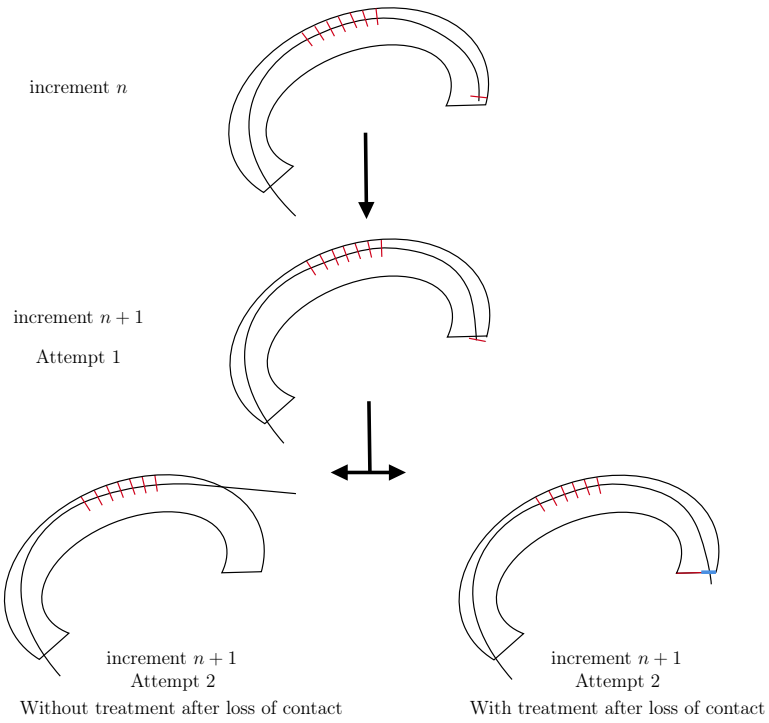

Figure 14: Sliding of the inner beam outside the limits of the outer beam. Penetrated sections are shown in red. At increment n, the last section placed along the inner beam is still inside the cavity. At increment $n+1$, it has slid outside the cavity. Bottom left: If no treatment is applied, the contact point at the tip of the inner beam is deactivated and it results in a sudden loss of contact; bottom right: the additional constraint is enforced between the section at the end of the outer beam (in red) and the surface of the inner beam.

Appendix B Figures for Example 2 with $E = 150$ MPa for the inner beam.

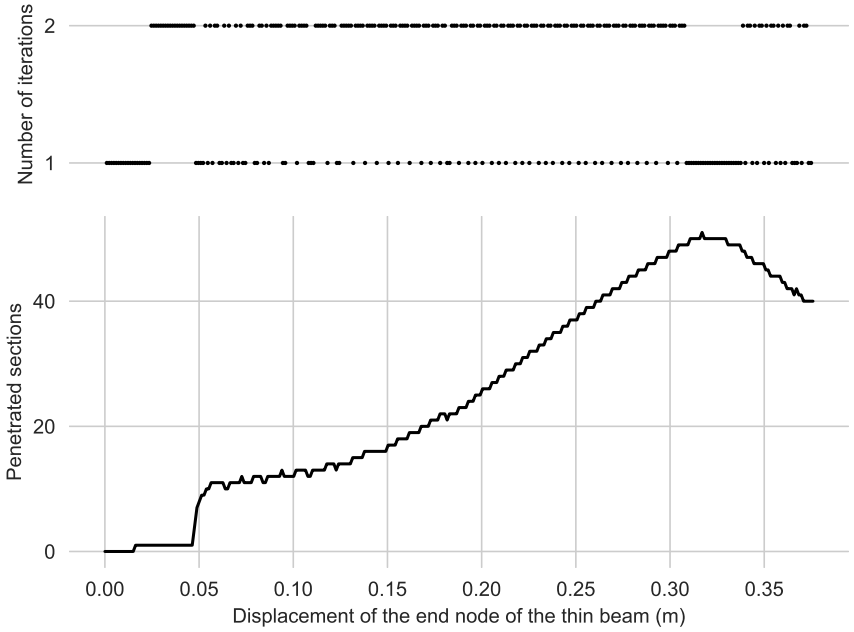

Figure 16: Example 2 with a stiffer inner beam: Top: number of global iterations to reach convergence criteria: $\left\| \underline{f}_{int} + \underline{r}_c - \underline{f}_{ext} \right\| < 10^{-8}$; Bottom: evolution of the number of contact interactions between sections of the thin beam and the surface of the outer beam.

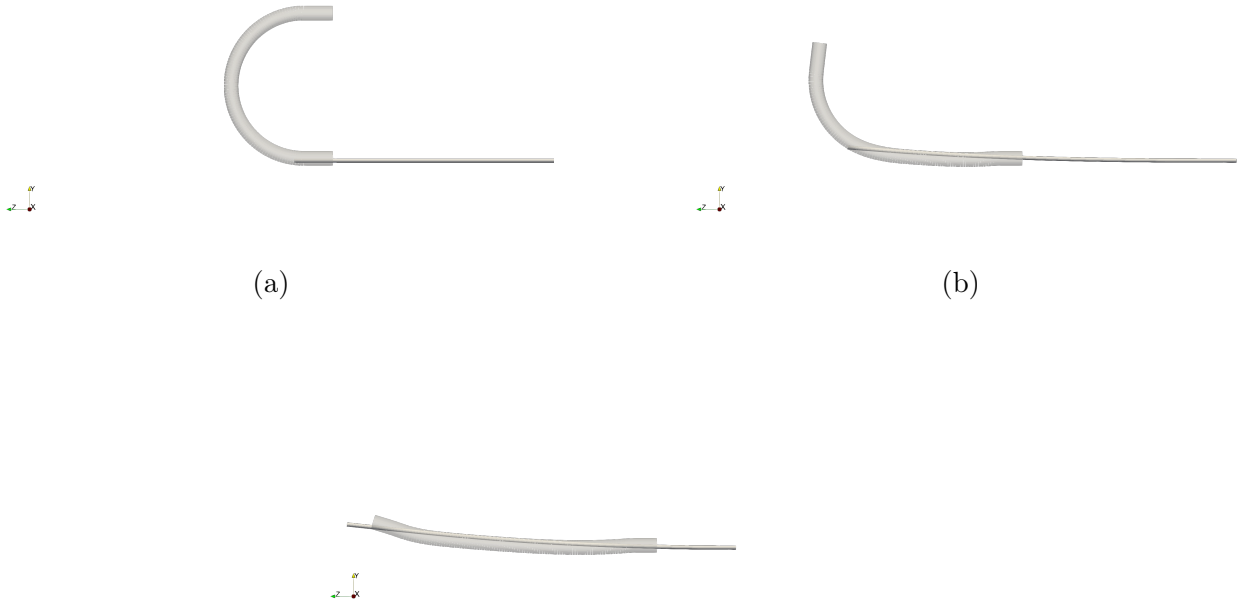

(a) (b)

(c)

Figure 15: Example 2 with a stiffer inner beam: (a) Initial configuration; (b) configuration halfway through the loading, and (c) final configuration.

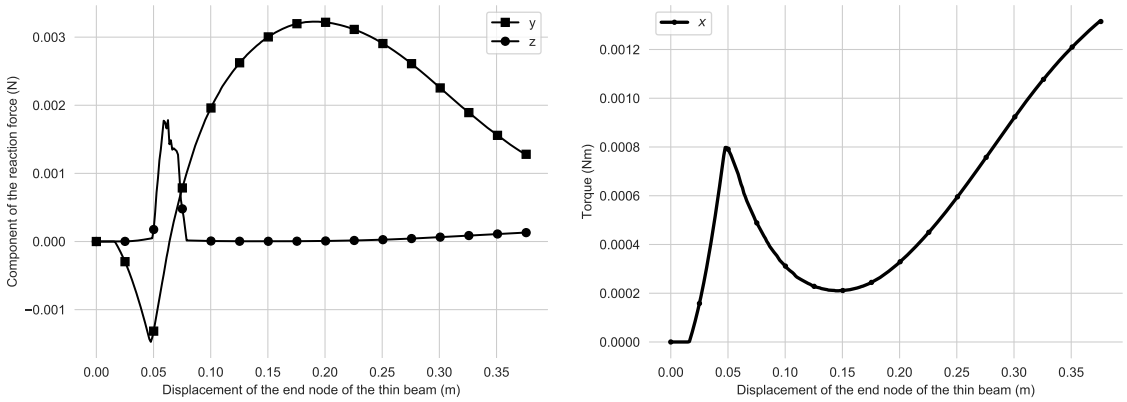

(a) (b)

Figure 17: Example 2 with a stiffer inner beam: components of the reaction force (a) and torque (b) at the prescribed end of the thin beam.

References

[1] Alderliesten, T., Konings, M.K., and Niessen, W.J. Simulation of minimally invasive vascular interventions for training purposes. *Computer Aided Surgery*, 9(1-2):3–15 (2004). doi:10.3109/10929080400006408.

[2] Alterovitz, R., Goldberg, K., and Okamura, A. Planning for steerable bevel-tip needle

insertion through 2D soft tissue with obstacles. In *Proceedings - IEEE International Conference on Robotics and Automation*, volume 2005, pages 1640–1645 (2005). ISBN 078038914X. doi:10.1109/ROBOT.2005.1570348.

[3] Coles, T.R., John, N.W., Gould, D., and Caldwell, D.G. Integrating haptics with augmented reality in a femoral palpation and needle insertion training simulation. *IEEE Transactions on Haptics*, 4(3):199–209 (2011). doi:10.1109/TOH.2011.32.

[4] Cotin, S., Delingette, H., and Ayache, N. Real-time elastic deformations of soft tissues for surgery simulation. *IEEE Transactions on Visualization and Computer Graphics*, 5(1):62–73 (1999). doi:10.1109/2945.764872.

[5] Courtecuisse, H., Allard, J., Kerfriden, P., Bordas, S.P., Cotin, S., and Duriez, C. Real-time simulation of contact and cutting of heterogeneous soft-tissues. *Medical Image Analysis*, 18(2):394–410 (2014). doi:10.1016/j.media.2013.11.001.

[6] Courtecuisse, H., Jung, H., Allard, J., Duriez, C., Lee, D.Y., and Cotin, S. GPU-based real-time soft tissue deformation with cutting and haptic feedback. *Progress in Biophysics and Molecular Biology*, 103(2-3):159–168 (2010). doi:10.1016/j.pbiomolbio.2010.09.016.

[7] Crisfield, M.A. and Jelenić, G. Objectivity of strain measures in the geometrically exact three-dimensional beam theory and its finite-element implementation. *Proceedings of the Royal Society of London. Series A: Mathematical, Physical and Engineering Sciences*, 455(1983):1125–1147 (1999). doi:10.1098/rspa.1999.0352.

[8] DiMaio, S.P. and Salcudean, S.E. Needle Insertion Modeling and Simulation. *IEEE Transactions on Robotics and Automation*, 19(5):864–875 (2003). doi:10.1109/TRA.2003.817044.

[9] Duriez, C., Cotin, S., Lenoir, J., and Neumann, P. New approaches to catheter navigation for interventional radiology simulation. *Computer Aided Surgery*, 11(6):300–308 (2006). doi:10.3109/10929080601090623.

[10] Duriez, C., Guébert, C., Marchal, M., Cotin, S., and Grisoni, L. Interactive simulation of flexible needle insertions based on constraint models. In *Lecture Notes in Computer Science (including subseries Lecture Notes in Artificial Intelligence and Lecture Notes in Bioinformatics)*, volume 5762 LNCS, pages 291–299 (2009). ISBN 3642042708. doi:10.1007/978-3-642-04271-3_36.

[11] Faure, F., Duriez, C., Delingette, H., Allard, J., Gilles, B., Marchesseau, S., Talbot, H., Courtecuisse, H., Bousquet, G., Peterlik, I., and Cotin, S. SOFA: A Multi-Model Framework for Interactive Physical Simulation. pages 283–321 (2012). doi:10.1007/8415_2012_125.

[12] Gay Neto, A., Pimenta, P.M., and Wriggers, P. A master-surface to master-surface formulation for beam to beam contact. Part I: frictionless interaction. *Computer Methods in Applied Mechanics and Engineering*, 303:400–429 (2016). doi:10.1016/j.cma.2016.02.005.

[13] Gay Neto, A., Pimenta, P.M., and Wriggers, P. A master-surface to master-surface formulation for beam to beam contact. Part II: Frictional interaction. *Computer Methods in Applied Mechanics and Engineering*, 319:146–174 (2017). doi:10.1016/j.cma.2017.01.038.

[14] Gay Neto, A. and Wriggers, P. Computing pointwise contact between bodies: a class of formulations based on master–master approach. *Computational Mechanics*, (0123456789) (2019). doi:10.1007/s00466-019-01680-9.

[15] Goury, O., Nguyen, Y., Torres, R., Dequidt, J., and Duriez, C. Numerical Simulation of Cochlear-Implant Surgery: Towards Patient-Specific Planning. In *Lecture Notes in Computer Science (including subseries Lecture Notes in Artificial Intelligence and Lecture Notes in Bioinformatics)*, volume 9900 LNCS, pages 500–507. Springer Verlag (2016). ISBN 9783319467191. doi:10.1007/978-3-319-46720-7_58.

[16] Ibrahimbegović, A., Frey, F., and Kožar, I. Computational aspects of vector-like parametrization of three-dimensional finite rotations. *International Journal for Numerical Methods in Engineering*, 38(21):3653–3673 (1995). doi:10.1002/nme.1620382107.

[17] Irschik, H. and Gerstmayr, J. A continuum-mechanics interpretation of Reissner's nonlinear shear-deformable beam theory. *Mathematical and Computer Modelling of Dynamical Systems*, 17(1):19–29 (2011). doi:10.1080/13873954.2010.537512.

[18] Jelenić, G. and Crisfield, M. Geometrically exact 3D beam theory: implementation of a strain-invariant finite element for statics and dynamics. *Computer Methods in Applied Mechanics and Engineering*, 171(1-2):141–171 (1999). doi:10.1016/S0045-7825(98)00249-7.

[19] Kazmitcheff, G. *Modélisation dynamique de l'oreille moyenne et des interactions outils organes pour la conception d'un simulateur appliqué à la chirurgie otologique*. Ph.D. thesis (2014).

[20] Khamdaeng, T., Luo, J., Vappou, J., Terdtoon, P., and Konofagou, E.E. Arterial stiffness identification of the human carotid artery using the stress-strain relationship in vivo. *Ultrasonics*, 52(3):402–411 (2012). doi:10.1016/j.ultras.2011.09.006.

[21] Konyukhov, A., Mrenes, O., and Schweizerhof, K. Consistent development of a beam-to-beam contact algorithm via the curve-to-solid beam contact: Analysis for the nonfrictional case. *International Journal for Numerical Methods in Engineering*, 113(7):1108–1144 (2018). doi:10.1002/nme.5701.

[22] Konyukhov, A. and Schweizerhof, K. *Computational Contact Mechanics*, volume 67 of *Lecture Notes in Applied and Computational Mechanics*. Springer Berlin Heidelberg, Berlin, Heidelberg (2013). ISBN 978-3-642-31530-5. doi:10.1007/978-3-642-31531-2.

[23] Korelc, J. Multi-language and multi-environment generation of nonlinear finite element codes. *Engineering with Computers*, 18(4):312–327 (2002). doi:10.1007/s003660200028.

[24] Korelc, J. and Wriggers, P. *Automation of Finite Element Methods*. Springer International Publishing, Cham (2016). ISBN 978-3-319-39003-1. doi:10.1007/978-3-319-39005-5.

[25] Laursen, T.A. and Simo, J.C. A continuum-based finite element formulation for the implicit solution of multibody, large deformation-frictional contact problems. *International Journal for Numerical Methods in Engineering*, 36(20):3451–3485 (1993). doi:10.1002/nme.1620362005.

[26] Lengiewicz, J., Korelc, J., and Stupkiewicz, S. Automation of finite element formulations for large deformation contact problems. *International Journal for Numerical Methods in Engineering*, 85(10) (2011). doi:10.1002/nme.3009.

[27] Lenoir, J., Cotin, S., Duriez, C., and Neumann, P. Interactive physically-based simulation of catheter and guidewire. *Computers and Graphics (Pergamon)*, 30(3):416–422 (2006). doi:10.1016/j.cag.2006.02.013.

[28] Magliulo, M., Lengiewicz, J., Zilian, A., and Beex, L.A.A. Non-localised contact between beams with circular and elliptical cross-sections. *Computational Mechanics* (2020).

[29] Magliulo, M., Zilian, A., and Beex, L.A.A. Contact between shear-deformable beams with elliptical cross sections. *Acta Mechanica* (2019). doi:10.1007/s00707-019-02520-w.

[30] Meier, C., Popp, A., and Wall, W.A. A finite element approach for the line-to-line contact interaction of thin beams with arbitrary orientation. *Computer Methods in Applied Mechanics and Engineering*, 308:377–413 (2016). doi:10.1016/j.cma.2016.05.012.

[31] Meier, C., Popp, A., and Wall, W.A. Geometrically Exact Finite Element Formulations for Slender Beams: Kirchhoff–Love Theory Versus Simo–Reissner Theory. *Archives of Computational Methods in Engineering*, 26(1):163–243 (2019). doi:10.1007/s11831-017-9232-5.

[32] Meier, C., Wall, W.A., and Popp, A. Geometrically Exact Finite Element Formulations for Curved Slender Beams: Kirchhoff-Love Theory vs. Simo-Reissner Theory. pages 1–92 (2016). doi:10.1007/s11831-017-9232-5.

[33] Meier, C., Wall, W.A., and Popp, A. A unified approach for beam-to-beam contact. *Computer Methods in Applied Mechanics and Engineering*, 315(August):972–1010 (2017). doi:10.1016/j.cma.2016.11.028.

[34] Mendoza, C. and Laugier, C. Simulating soft tissue cutting using finite element models. In *Proceedings - IEEE International Conference on Robotics and Automation*, volume 1, pages 1109–1114. Institute of Electrical and Electronics Engineers Inc. (2003). doi:10.1109/robot.2003.1241741.

[35] Romero, I. The interpolation of rotations and its application to finite element models of geometrically exact rods. *Computational Mechanics*, 34(2):121–133 (2004). doi:10.1007/s00466-004-0559-z.

[36] Secoli, R. and Baena, F.R.Y. Adaptive path-following control for bio-inspired steerable needles. In *Proceedings of the IEEE RAS and EMBS International Conference on Biomedical Robotics and Biomechatronics*, volume 2016-July, pages 87–93. IEEE Computer Society (2016). ISBN 9781509032877. doi:10.1109/BIOROB.2016.7523603.

[37] Simo, J. and Vu-Quoc, L. A three-dimensional finite-strain rod model. part II: Computational aspects. *Computer Methods in Applied Mechanics and Engineering*, 58(1):79–116 (1986). doi:10.1016/0045-7825(86)90079-4.

[38] Simo, J. and Vu-Quoc, L. A Geometrically-exact rod model incorporating shear and torsion-warping deformation. *International Journal of Solids and Structures*, 27(3):371–393 (1991). doi:10.1016/0020-7683(91)90089-X.

[39] Trivisonne, R., Cotin, S., Kerrien, E., Trivisonne, R., Cotin, S., and Kerrien, E. Constrained Stochastic State Estimation for 3D Shape Reconstruction of Catheters and Guidewires in Fluoroscopic Images (2019).

[40] Wriggers, P. *Computational Contact Mechanics*. Springer Berlin Heidelberg, Berlin, Heidelberg (2006). ISBN 978-3-540-32608-3. doi:10.1007/978-3-540-32609-0.

[41] Wriggers, P. and Zavarise, G. On Contact Between Three-Dimensional Beams Undergoing Large Deflections. *Communications in Numerical Methods in Engineering*, 13(6):429–438 (1997). doi:10.1002/(SICI)1099-0887(199706)13:6<429::AID-CNM70>3.0.CO;2-X.

[42] Wu, W. and Heng, P.A. An improved scheme of an interactive finite element model for 3D soft-tissue cutting and deformation. *The Visual Computer*, 21(8-10):707–716 (2005). doi:10.1007/s00371-005-0310-6.

[43] Zavarise, G. and Wriggers, P. Contact with friction between beams in 3-D space. *International Journal for Numerical Methods in Engineering*, 49(8):977–1006 (2000). doi:10.1002/1097-0207(20001120)49:8<977::AID-NME986>3.0.CO;2-C.